Novel Red-Emitting Sr(Lu, Sc)2O4: Eu2+ Transparent Ceramics for Laser-Driven Lighting and Display

Journal:	*SCIENCE CHINA Materials*
Manuscript ID	SCMs-2026-2786.R2
Manuscript Type:	Article
Date Submitted by the Author:	29-Oct-2026
Complete List of Authors:	Hu, Dahai; Fujian Normal University Lin, Shisheng; Fujian Normal University Zheng, Yongping; Fujian Normal University Zeng, Lingwei An , Ran ; Fujian Normal University Xie, Rong ; Fujian Normal University Zhou, Zhehong Chen, Bin ; Fujian Normal University Li , Xiaoyan ; Fujian Jiangxia University Huang, Feng; Fujian Normal University Xie, an; Xiamen University of Technology Chen, Daqin; Fujian Normal University,
Keywords:	Phosphors, Luminescent ceramics, Red-emitting color converters, Laser-driven lighting and display
Speciality:	Optoelectronic Materials



Novel Red-Emitting $Sr(Lu, Sc)_2O_4$: Eu^{2+} Transparent Ceramics for Laser-Driven Lighting and Display

Dahai Hu[1], Shisheng Lin[1*], Yongping Zheng[1], Lingwei Zeng[2], Ran An[1], Rong Xie[1], Zhehong Zhou[1], Bin Chen[1], Xiaoyan Li[3*], Feng Huang[1], An Xie[4], Daqin Chen[1,5*]

[1]College of Physics and Energy, Fujian Provincial Key Laboratory of Quantum Manipulation and New Energy Materials, Fujian Normal University, Fuzhou, Fujian, 350117, P. R. China

[2]School of Chemistry and Chemical Engineering, Key Laboratory of Theoretical Organic Chemistry and Functional Molecule of Ministry of Education, Hunan University of Science and Technology, Xiangtan, Hunan, 411201, P. R. China

[3]College of Electronics and Information Science, Fujian Jiangxia University, Fuzhou, Fujian, 350108, P. R. China

[4]School of Materials Science and Engineering, Key Laboratory of Functional Materials and Applications of Fujian Province, Xiamen University of Technology, Xiamen, Fujian, 361024, P. R. China

[5]Fujian Provincial Engineering Technology Research Center of Solar Energy Conversion and Energy Storage, Fuzhou, Fujian, 350117, P. R. China

*Corresponding author (email: linshisheng@fjnu.edu.cn; xyli@fjjxu.edu.cn; dqchen@fjnu.edu.cn)

For Review Only

ABSTRACT

Highly efficient and robust red-emitting ceramics are in urgent demand for advanced optoelectronic applications. In this work, a series of red-emitting $Sr(Lu_{1-x}Sc_x)_2O_4$: Eu^{2+} (SLS: Eu^{2+}) solid solution phosphor ceramics (PCs) were successfully fabricated, exhibiting intense red emission (611-643 nm, FWHM: 73-83 nm), desired thermal stability (47.3 %@200 °C), excellent double-85 reliability (94.6 %@1200 h), and strong resistance to high-power blue laser irradiation (96.3 %@120 min under 15 W/5.90 W·mm^{-2} excitation). Combined theoretical calculations and

experimental analyses reveal that partial substitution of Lu^{3+} by Sc^{3+} leads to contraction and enhanced distortion of the [Sc/Lu/EuO_6] octahedra, accompanied by increased Eu-O bond covalency, which collectively contributes to the observed spectral modulation and performance enhancement. Furthermore, prototype laser-driven lighting and display devices based on the SLS: Eu^{2+} PCs were constructed, delivering neutral-white emission with a correlated color temperature (CCT) of 4891 K and a high color rendering index (Ra = 90.2), while achieving a wide color gamut beyond 100 % NTSC. Evidently, this work provides valuable insights for the design of high-performance red-emitting materials for laser-driven lighting and display technologies.

Keywords: Phosphors; Luminescent ceramics; Red-emitting color converters; Laser-driven lighting and display

INTRODUCTION

Driven by high demands for medical lighting, automotive/aviation illumination, as well as high-end projection systems, solid-state lighting technologies - the core of modern lighting and display platforms - are continuously advancing toward higher power operation, enhanced stability, improved luminous efficiency, higher color rendering index, and broader color gamut performance [1-5]. Among candidates, the “laser diodes (LDs) + color converters” has emerged as a promising approach for high-performance solid-state lighting. This is primarily attributed to the intrinsic immunity LDs to efficiency droop, which enables the development of lighting systems that simultaneously achieve high brightness, high efficiency, and compact form factors [6-8]. However, the corresponding color converters must withstand prolonged high-power-density photon irradiation while efficiently dissipating heat to suppress luminescence quenching and maintain optical performance. Evidently, the development of novel color converters featuring high luminous efficiency and robust resistance to laser irradiation is imperative. Due to excellent

For Review Only

chemical stability, high thermal conductivity, and tunable microstructural characteristics, phosphor ceramics (PCs) have emerged as particularly promising candidates among available materials [9-12].

From the perspective of host lattices, PCs based on $Y_3Al_5O_{12}$: Ce^{3+} (YAG: Ce^{3+}) and $Lu_3Al_5O_{12}$: Ce^{3+} (LuAG: Ce^{3+}) have been extensively studied as efficient yellow- and green-emitting color converters [13-15]. However, primarily due to the absence of essential red-emitting components, lighting systems employing such garnet-structured PCs typically exhibit excessively cold correlated color temperatures (CCTs > 6500 K) and relatively low color rendering indices (CRI < 75) when coupled with blue or violet LDs, thus significantly hindering the advancement of laser-driven solid-state lighting toward high-end applications [16-20]. Furthermore, although fluorides (e.g., K_2SiF_6: Mn^{4+}), perovskite quantum dots (e.g., $CsPb(Br/I)_3$), and nitride phosphors (e.g., $CaAlSiN_3$: Eu^{2+}) are widely regarded as the leading candidates for red-emitting PCs, each system still encounters distinct challenges, including environmental concerns, insufficient chemical stability, high material costs, and stringent synthesis conditions [21-23]. In contrast, oxide-based systems offer notable advantages in terms of superior chemical stability, lower raw material cost, and more accessible fabrication routes [1, 3, 12, 24], which enables red-emitting oxide PCs to fully meet the requirements for industrial-scale production and hold significant potential for commercial applications [3-5].

Regarding the luminescent centers, the emission of Eu^{2+} originates from the parity-allowed $4f^65d^1 \rightarrow 4f^7$ transition, endowing Eu^{2+}-activated color converters with intrinsically high absorption coefficients [25-27]. Nevertheless, Eu^{2+}-activated oxides typically exhibit blue or green emission due to the relatively weak crystal-field strength of oxide hosts [28, 29]. When Eu^{2+} occupies a coordination environment with a sufficiently strong crystal field, the 5d energy levels are significantly lowered, resulting in a pronounced redshift of the emission band toward the orange or even red spectral region. To date, only a limited number of Eu^{2+}-activated red-emitting oxide phosphors have been reported. Representative examples include $Sr_3TaO_{5.5}$: Eu^{2+} (λ_{em} = 620 nm, FWHM = 73 nm) and $Mg_2Al_4Si_5O_{18}$:Eu^{2+} (λ_{em} = 625 nm, FWHM = 103 nm). However, their limited spectral modulation capability (<630 nm), hinders the ability to meet the stringent requirements of next-generation high-quality white lighting and wide-color-gamut display

For Review Only

technologies [29, 30]. Therefore, the development of robust oxide-based Eu^{2+}-activated red-emitting PCs with deeper-red emission remains highly desirable.

Herein, we fabricated oxide-based solid solution red-emitting $Sr(Lu_{1-x}Sc_x)_2O_4$: yEu^{2+} ($0 \le x \le 0.4$, $0.001 \le y \le 0.02$) (SLS: Eu^{2+}) PCs for the first time. Benefiting from the rigid crystal structure, Sc-induced enhanced centroid shift and crystal-field splitting, and high relative density (96 %), SLS: Eu^{2+} PCs exhibit red emission peaking at 611-643 nm with a FWHM of 73-83 nm, desired thermal stability (47.3 %@200 °C), excellent double-85 stability (94.6 %@1200 h), and outstanding resistance to blue laser irradiation (96.3 %@120 min, 15 W/5.90 W·mm^{-2}). Furthermore, by combining the SLS: Eu^{2+} PC with commercial yellow-emitting YAG: Ce^{3+} PC, a prototype lighting device achieved high-quality neutral white light with a low CCT (4891 K) and significantly improved CRI (Ra = 90.2). Meanwhile, a laser-driven display prototype was constructed through a patterned integration of the SLS: Eu^{2+} PC, commercial green-emitting β-SiAlON: Eu^{2+} PC, and a 450 nm LD, achieving an ultrawide color gamut covering 100.7 % NTSC standard (Table S1). This work facilitates the development of red-emitting color converters and their applications in LD-driven lightings and displays.

EXPERIMENTAL SECTION

Preparation of phosphor ceramics

A series of $Sr(Lu_{1-x}Sc_x)_2O_4$: yEu^{2+} ($0 \le x \le 0.4$) ($0.001 \le y \le 0.02$) (SLS: Eu^{2+}) transparent ceramics were synthesized via a gas pressure sintering technology, where the used raw materials were $SrCO_3$ (Innochem Corporation, Beijing, China, 99.95%), Lu_2O_3 (Innochem Corporation, Beijing, China, 99.99%), Sc_2O_3 (Innochem Corporation, Beijing, China, 99.99%), and Eu_2O_3 (Innochem Corporation, Beijing, China, 99.99%). The precursor powders were accurately weighed in air and subsequently ball-milled in ethanol at 300 r/min for 24 h. After that, the slurry was dried at 70 °C for 10 h and sieved using a 200-mesh screen. The mixtures were then calcined in a muffle furnace at 600 °C for 20 h to eliminate impurities. The resulting green bodies were pressed into shape

For Review Only

using a stainless-steel mold (Φ = 30 mm) under an axial load of 10 MPa, followed by cold isostatic pressing (CIP) at 260 MPa for 20 min. The pressed green bodies underwent additional calcination in a muffle furnace at 800 °C for 20 h to remove any remaining organic residues. Final sintering was performed in a gas pressure furnace (Nanjing Boyuntong Instrument Co., Ltd., China) under a nitrogen-hydrogen mixed atmosphere (90 % N_2+10 % H_2) at 1550-1580 °C for 30 h. The samples were annealed in high purity nitrogen (99.999 %) at 800 °C for 4 h. Upon cooling, both sides of the samples were polished for subsequent characterization.

Preparation of lighting prototypes

The ceramic wheel was prepared of YAG: Ce^{3+} ceramic machined into a specific size, which is driven by a motor to keep the rotation speed of 3000 r/min, and driven by a 450nm laser to emit white light, which is combined as lighting source 1. SLS: Eu^{2+} red-emitting ceramics were further supplemented to prepare lighting source 2.

Preparation of laser-driven display prototypes

The display lighting source 1 continues to be functioned by the lighting source 1 based on commercial YAG: Ce^{3+} ceramic. SLS: Eu^{2+} red-emitting ceramics was combined with commercial narrow-band green-emitting β-SiAlON: Eu^{2+} PC to form a composite wheel, and maintained the same rotational speed and laser drive, as a display lighting source 2.

Characterization

Microscopic morphologies of the SLS: Eu^{2+} ceramics were examined via scanning electron microscopy (SEM, COXEM EM-30) coupled with energy dispersive spectroscopy (EDS) (Hitachi SU8220). Phase purity and crystallographic structure were analyzed using an X-ray polycrystalline

For Review Only

powder diffractometer (SmartLab Rigaku) with Cu Kα radiation (λ = 0.154 nm), operating at 40 kV and 30 mA, and scanning at a rate of 5 °/min over a 2θ range of 10°-90°. The thermal conductivity of the phosphor ceramic was studied by the laser flash method (Netzch, LFA-457, Germany). Photoluminescence emission (PL), photoluminescence excitation (PLE), decay curves, and photoluminescence quantum yield (PLQY) were measured using a fluorescence spectrometer (FLS1000, Edinburgh Instruments, UK). Temperature-dependent PL spectra were also obtained with this spectrometer, using a heating attachment (THMS600E, Linkam Scientific Instruments). The samples were heated to 200 ℃ in 25 ℃ intervals at a rate of 5 ℃/min, with a 5-minute holding period at each temperature to achieve thermal equilibrium. Photometric and colorimetric parameters under 450 nm laser excitation were recorded using a custom-built laser illumination system comprising an integrating sphere (30 cm in diameter, Labsphere, Inc., USA), a blue laser source (LSR-PS-FA, Lasever, China), and a CCD spectrometer (OHSP-350M, Hopoocolor Technology Co., Ltd., China) operating in reflection mode. The laser spot size was adjusted to a 2.543 mm^2 area using a lens. Thermographic imaging was captured using an infrared thermal camera (TiS75, Fluke, USA), positioned 15 cm from the sample.

Theoretical calculations

Density functional theory (DFT) calculations are performed using the Vienna ab initio simulation package (VASP). The formation energy, geometry optimizations and charge distribution calculations of the investigated crystal structures were performed using DFT and the generalized gradient approximation (GGA)-Perdew-BurkeErnzerhof (PBE) exchange-correlation functional in the VASP package. The Sr ($[Kr]5s^2$), Lu ($[Xe]4f^{14}5d^16s^2$), Sc ($[Ar]3d^14s^2$), O ($[He]2s^22p^4$) and Eu ($[Xe]4f^76s^2$) were treated as valence electrons, and the projector augment wave (PAW)

For Review Only

pseudopotential method with a kinetic energy cutoff of 450 eV on a 5×2×3 Gamma-center *k*-point mesh for 2×2×1 supercell was used to describe the interactions with the cores. All of the atoms are fully relaxed until the residual forces on each of them are less than 0.02 eV/Å, and the energy convergence criterion are set to 10^{-6} eV.

RESULTS AND DISCUSSION

Morphology and structure

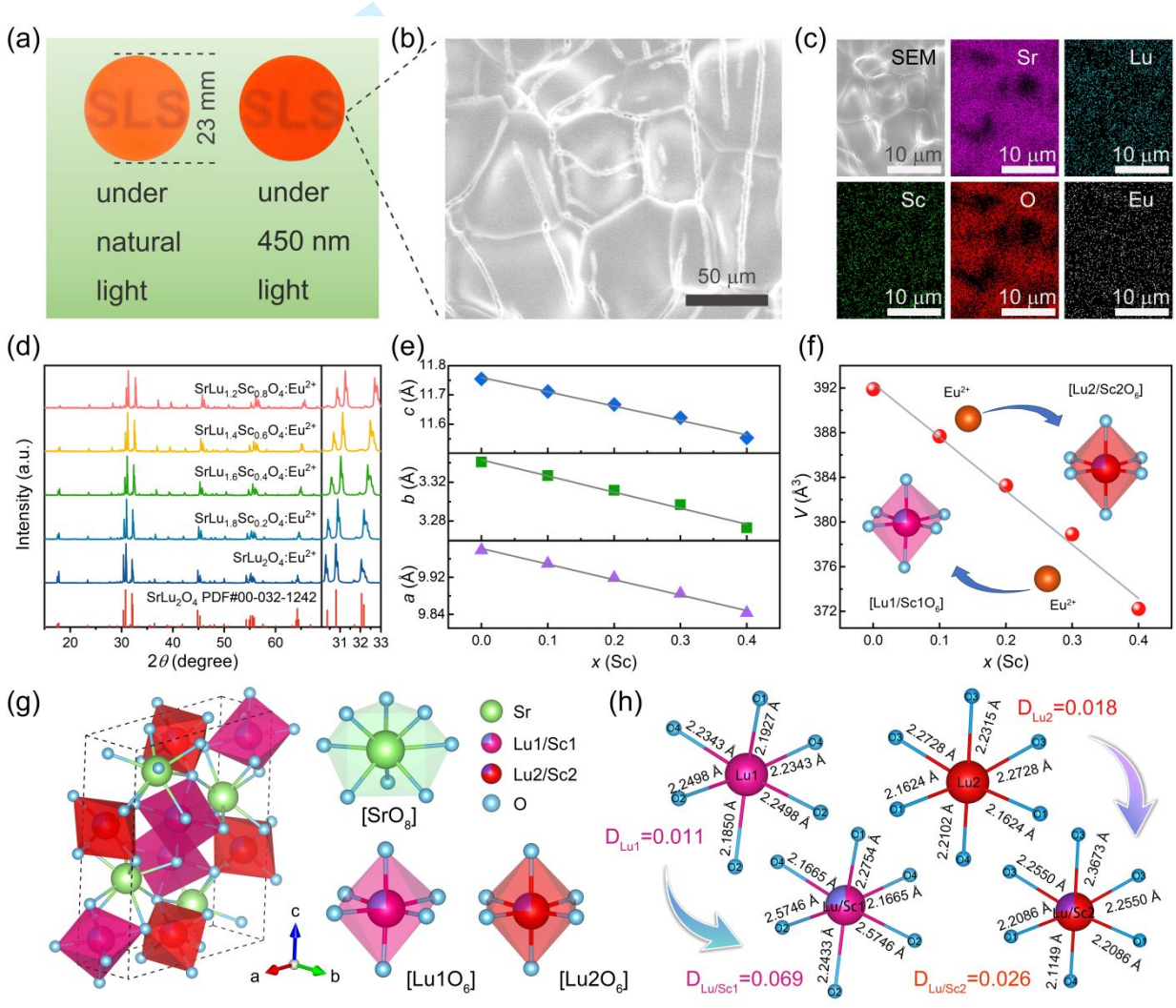


Figure 1 Phase identification, microstructure, and crystal structure of SLS: Eu^{2+} PCs. (a) Photographic images of SLS: Eu^{2+} PCs (thickness: 0.36 mm) under natural light and blue-light irradiation. (b) SEM image and (c) corresponding EDS elemental mapping illustrating the spatial distribution of Sr, Lu, Sc, O, and Eu in SLS: Eu^{2+} PCs. (d) XRD patterns and enlarged XRD patterns at 2θ = 30.2°-33° of $SL_{1-x}S_x$: Eu^{2+} ($0 \le x \le 0.4$) PCs. (e)

Evolution of lattice parameters and (f) unit cell volume (V) as a function of Sc^{3+} doping concentration; the insets in (f) present schematic illustration of Eu^{2+} occupancy [Lu/ScO_6] sites. (g) Schematic representation of the crystal structure of SLS. (h) Local coordination environments of the Lu1/Lu2 crystallographic sites.

Red-emitting $Sr(Lu_{1-x}Sc_x)_2O_4$: Eu^{2+} ($0 \leq x \leq 0.4$) (SLS: Eu^{2+}) solid solution PCs were synthesized via a high-temperature solid-state reaction under vacuum using oxide/carbonate raw materials (Figs S1 and S2). The SLS: Eu^{2+} PCs exhibit good transparency and emit intense red light upon blue light excitation (Fig. 1a; Figs S3 and S4). SEM images of SLS: Eu^{2+} PCs reveal irregular polygonal grains with clear grain boundaries, no obvious pores or precipitated secondary phases (Fig. 1b and Fig. S5), demonstrating favorable densification of the ceramics. The samples exhibit a high relative density over 91 %, reaching 96 % (Fig. S6). Additionally, the elemental mapping images reveal that Sr, Lu, Sc, O, and Eu are homogeneously distributed in the SLS: Eu^{2+} ceramics (Fig. 1c and S7). The X-ray diffraction (XRD) patterns match well with the standard $SrLu_2O_4$ (JCPDS#32-1242) [31], confirming that all the as-prepared SLS: Eu^{2+} samples are of pure phase (Fig. 1d). Notably, the relative difference in ionic radii between the two cations is 15.6 % (Sc^{3+} ($R_{CN=6}$ = 0.745 Å); Lu^{3+} ($R_{CN=6}$ = 0.861 Å)) [32]. Constrained by the Hume-Rothery rules [33], the $Sr(Lu_{1-x}Sc_x)_2O_4$: Eu^{2+} ($0 \leq x \leq 1$) system tends to form a limited solid solution, and full-range infinite mutual solubility cannot be achieved. Single phase $SrLu_2O_4$ is retained at low Sc substitution levels, while impurity phases precipitate once Sc doping surpasses the solid solution limit. This is corroborated by our preliminary XRD results (Fig. S8). Considering both phase purity and luminescence performance comprehensively, the composition range of $0 \leq x \leq 0.4$ was selected for this investigation. To obtain detailed structural information, Rietveld refinement of XRD pattern of $SL_{1-x}S_x$: Eu^{2+} ($0 \leq x \leq 0.4$) was conducted (Fig. S9 and Table S2), and relevant atomic coordinates, occupancy and isotropic thermal displacement parameters are

For Review Only

presented in Tables S3-S7. With the increased Sc^{3+} doping concentration (Fig. 1e, f), the cell parameters (V, *a*, *b*, *c*) of SLS: Eu^{2+} decrease linearly because the ionic radius of Sc^{3+} ($R_{CN=6}$ = 0.745 Å) is smaller than that of Lu^{3+} ($R_{CN=6}$ = 0.861 Å), which simultaneously intensifies the octahedral distortion of [Lu1/Sc1O_6] and [Lu2/Sc2O_6] polyhedra (distortion indices rise from D = 0.011/0.018 to D = 0.069/0.026, respectively) (Fig. 1g, h; Fig. S10; Equation S1).

Luminescence performance and stability

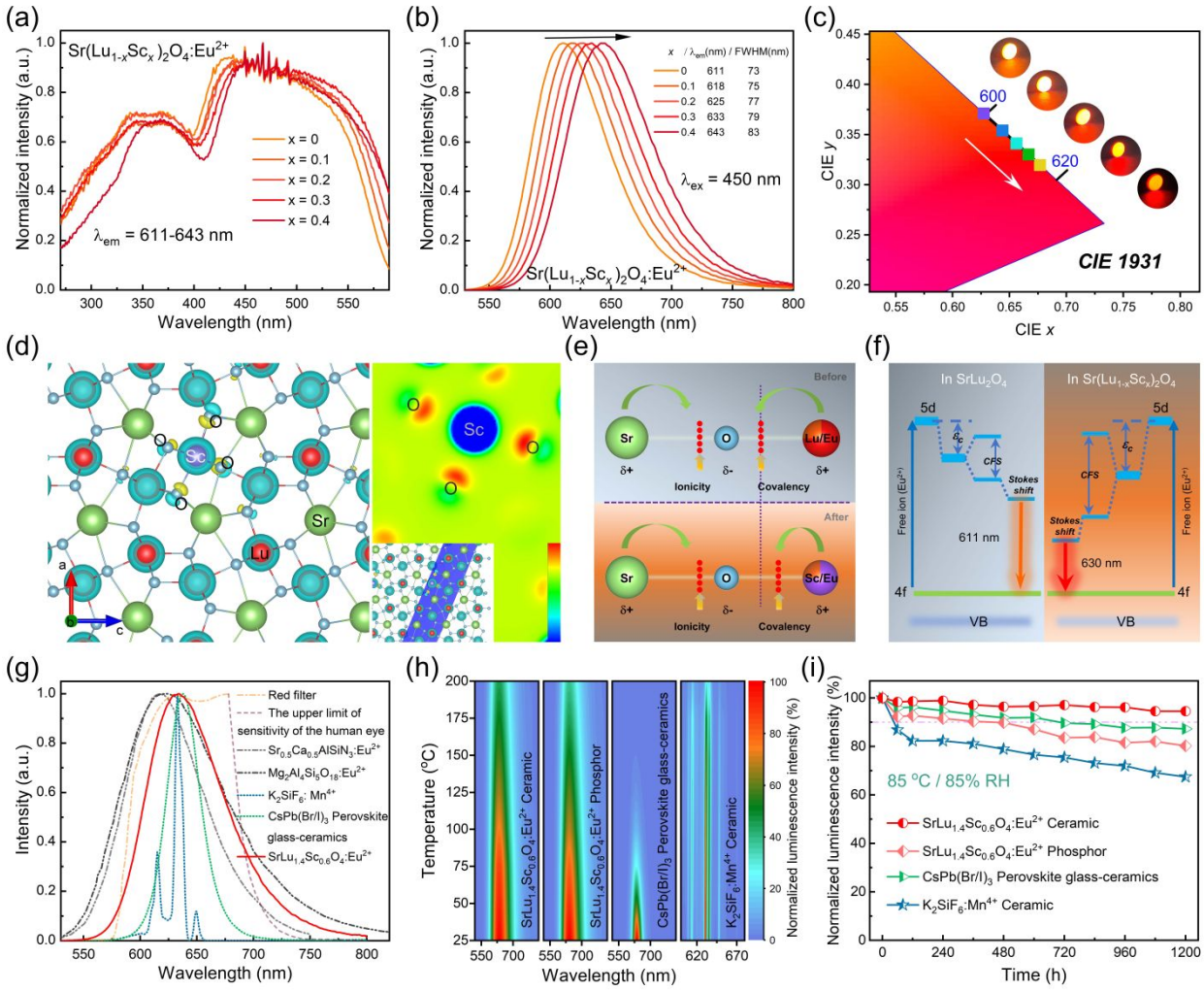


Figure 2 Luminescence properties, mechanism, and stability of SLS: Eu^{2+} PCs. (a) PLE, (b) PL spectra, and (c) CIE chromaticity coordinates of $SL_{1-x}S_x$: Eu^{2+} ($0 \le x \le 0.4$) PCs. (d) Differential charge density distribution of the SLS: Eu^{2+}. (e) Schematic illustration of electronegativity variation. (f) Energy transfer mechanism diagram of Eu^{2+} in the SLS host lattice. (g) Comparative PL spectra of $SrLu_{1.4}Sc_{0.6}O_4$: Eu^{2+} PC and representative red-

emitting color converters. (h) Temperature-dependent two-dimensional contour maps of PL spectra, with the luminescence intensity normalized to a range of 0-100. (i) Stability evaluation under 85 °C/85% RH accelerated aging conditions for $SrLu_{1.4}Sc_{0.6}O_4$: Eu^{2+} PC, $SrLu_{1.4}Sc_{0.6}O_4$: Eu^{2+} phosphor powders, K_2SiF_6: Mn^{4+} PC, and $CsPb(Br/I)_3$ perovskite glass-ceramics.

Furthermore, the luminescence performance of the corresponding samples was characterized. The luminescence intensity of $SrLu_2O_4$: yEu^{2+} ($0.001 \leq y \leq 0.02$) PCs is significantly affected by the Eu doping content, with the optimal doping concentration of y = 0.004, emitting at 611 nm under 450 nm excitation (Figs S11-S13). Under 450 nm excitation, the internal quantum efficiency (IQE), absorption efficiency (AE), and external quantum efficiency (EQE) of $SrLu_2O_4$: $0.004Eu^{2+}$ PC are 66.9 %, 47.3 %, and 31.7 %, respectively (Fig. S14). As shown in Fig. S15, at low Eu doping content, the emission band of $SrLu_2O_4$: $0.004Eu^{2+}$ can be well deconvoluted into two Gaussian peaks [34-38], where the more intense Eu1(Lu1) emission peak is located at 16486 cm^{-1} (606 nm), the weaker Eu2(Lu2) emission peak is located at 15550 cm^{-1} (643 nm). However, $SrLu_2O_4$:$0.004Eu^{2+}$ PC exhibit a pronounced mismatch between their emission peak wavelength and the optimal red spectral region (620-650 nm) required for high-performance lighting and display applications [38-41].

Although the overall XRD patterns remain analogous benefiting from the favorable Sc^{3+}/Lu^{3+} ionic radius matching, continuous peak shifts and lattice shrinkage occur upon Sc^{3+} substitution, which modulate local crystal field environments and further tailor the luminescence properties of Eu^{2+}. Figs 2a-c, Figs S16 and S17 present the photoluminescence (PL) properties of $SL_{1-x}S_x$: $0.004Eu^{2+}$ ($0 \leq x \leq 0.4$) PCs. The photoluminescence excitation (PLE) spectra monitored at emission peaks (611-643 nm) exhibit a broad band from 350 nm to 600 nm, originating from the

For Review Only

$4f^7 \rightarrow 4f^6 5d$ transitions of Eu^{2+} ions [2, 35, 42]. With the increased Sc doping content, the 5d energy level of SLS: Eu^{2+} shifts downward, causing the excitation peak to gradually redshift to 450 nm and achieving better spectral matching with commercial blue LD. Under 450 nm excitation, the emission peaks of $SL_{1-x}S_x$: $0.004Eu^{2+}$ ($0 \leq x \leq 0.4$) gradually shift from 611 nm to 643 nm with the FWHM varying from 73 nm to 83 nm (Fig. 2b, c) and continuous improvement in color purity (Table S8). Generally, the emission energy distribution of Eu^{2+} is related to the crystal field splitting (ε_{cfs}), centroid shift (ε_c), and Stokes shift. (1) The ε_{cfs} value can be calculated by the equation below [35]:

$$\varepsilon_{cfs} = \beta_{poly}^{Q} R_{av}^{-2} = \beta_{poly}^{Q} \left[\frac{1}{N} \sum_{i=1}^{CN} (R_i - 0.6(R_M - R_{Ln})) \right]^{-2}, \quad (1)$$

Where Q equals 2+ for Eu^{2+}, the β_{poly}^{Q} (0.79×10^9 $cm^{-1} \cdot pm^2$) relies on the type of coordination polyhedron, with R_i represents the individual bond lengths to the coordinating anions in the unrelaxed lattice, R_M the cation radius, and R_{Ln} the ionic radius of the luminescent center [35]. The R_{av} values calculated for Eu^{2+} in the Sc^{3+} sites ($R_{av,\,Sc1}$ = 2.1474 Å, $R_{av,\,Sc2}$ = 2.1526 Å) are smaller than in the Lu^{3+} sites ($R_{av,\,Lu1}$ = 2.2243 Å, $R_{av,\,Lu2}$ = 2.2187 Å), resulting in a greater ε_{cfs} for Eu^{2+} in the Sc^{3+} sites. (2) The increased distortion (D_1: 0.011→0.069, D_2: 0.018→0.026) of the coordination polyhedron at the luminescence centers aggravates crystal field splitting (Fig. S10) [35, 43], jointly enhancing the spectral redshift. (3) In a ligand polarization model, the centroid shift (ε_c) of the 5d configuration is determined by coordination number, bond lengths, and the polarizability of adjacent anions. The relationship between polarizability α_{sp} and the ε_c is given by the equation below [2, 44]:

$$\frac{1}{\alpha_{sp}} = \frac{1.79 \times 10^{13}}{\varepsilon_c} \sum_{i=1}^{N} \frac{1}{(R_i - f\Delta R)^6}, \quad (2)$$

mater.scichina.com

For Review Only

Where ΔR represents the difference between the ionic radius of luminescent center in the crystal and the cation it replaces, α_{sp} exhibits a negative correlation with the bonding strength toward oxygen ligands [2, 44]. Due to its higher electronegativity (1.36) relative to Lu^{3+} (1.26), Sc^{3+} more strongly attracts the outer electron cloud of O^{2-} ligands and confers greater covalent character upon the Sc-O bonds, giving rise to a larger ε_c parameter for Eu^{2+} at Sc^{3+} sites than at Lu^{3+} sites. As shown in the differential charge density distribution in Fig. 2d, the charge characteristics of Sr sites, M (Lu/Sc/Eu) sites and bridging O atoms are displayed. Compared with the original structural model (M = Lu^{3+}), substitution of Lu by Sc shifts electrons of M-O bonds toward M atoms (Fig. 2d, e), which enhances the covalency of Sc-O bonds [44]. The nephelauxetic effect governs the 5d electronic energy level distribution of Eu^{2+}, and can be effectively strengthened by elevated bond covalency. These synergistically working factors (Fig. 2f) enable Sc-substituted SLS: Eu^{2+} red-emitting PCs to exhibit more red-shifted emission peaks relative to most Eu^{2+}-activated red-emitting color converters (Fig. 2g; Figs S18 and S19) [45-47].

In addition, thermal stability is crucial for laser-driven color converters in device applications [48, 49]. At 200 °C (Fig. 2h; Figs S20 and S21), the luminescent intensities of SLS: Eu^{2+} PC bulk, SLS: Eu^{2+} phosphor powder, $CsPb(Br/I)_3$ perovskite glass-ceramics bulk, and K_2SiF_6: Mn^{4+} PC were 47.3 %, 40.1 %, 0.7 %, and 30.4 % of their corresponding initial intensities, respectively. These results reveal that SLS: Eu^{2+} red-emitting PCs retain favorable red emission characteristics even at elevated operating temperatures.

Moreover, the $SrLu_{1.4}Sc_{0.6}O_4$: Eu^{2+} ceramic exhibited outstanding resistance to aging, retaining over 94.6 % of its initial PL intensity after an accelerated aging test exceeding 1200 h under harsh conditions (85 °C/85 % RH; Fig. 2i and S22), not only surpassing the stringent

For Review Only

commercial operational lifetime requirements [50, 51], but also significantly outperforming K_2SiF_6: Mn^{4+} PC (67.4 % @1200 h), $CsPb(Br/I)_3$ perovskite glass-ceramic (87.2 % @1200 h), and $SrLu_{1.4}Sc_{0.6}O_4$: Eu^{2+} phosphor (80.3 % @1200 h).

Performance and stability under laser-driven

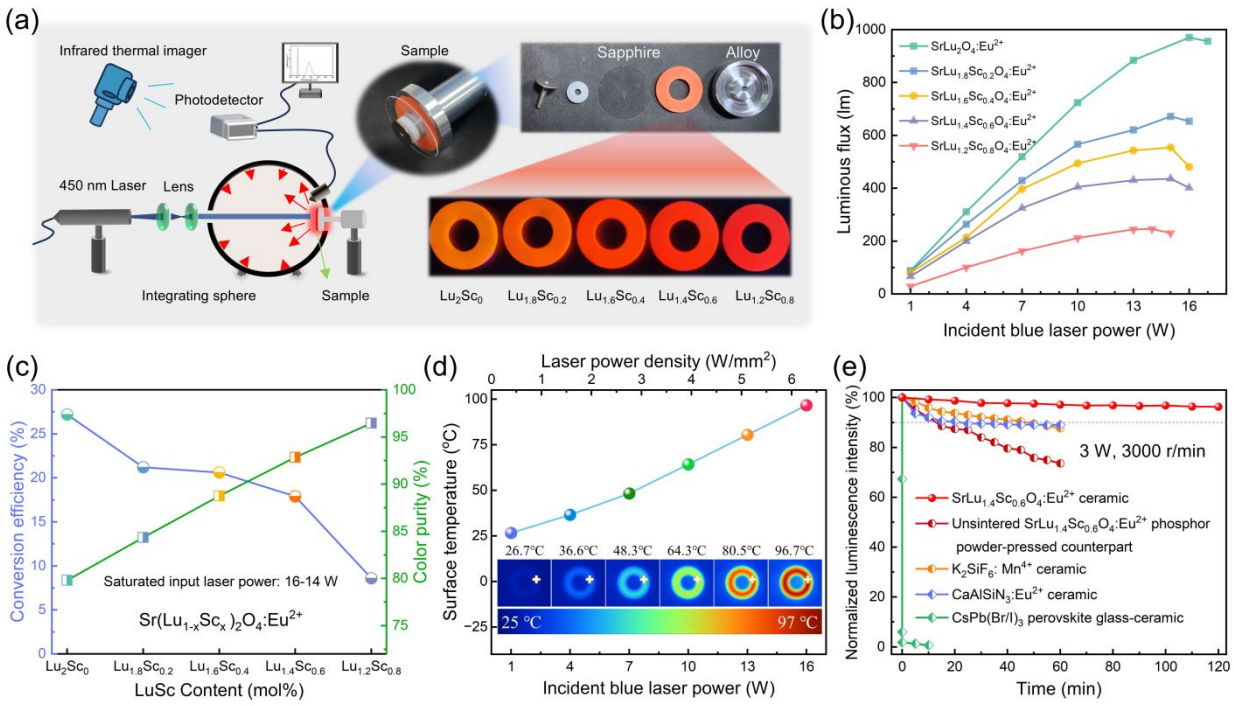


Figure 3 The optical performance of SLS: Eu^{2+} PCs under 450 nm LD excitation. a) Schematical illustration of the self-built laser illumination system. b) P_{in}-dependent LF in rotation mode. c) Corresponding conversion efficiency and color purity when luminescence saturation. d) Temperature evolution at the laser-irradiated spot of the $SrLu_{1.4}Sc_{0.6}O_4$: $0.004Eu^{2+}$ PC in rotational mode after 5 min of blue laser irradiation at different power; insets show the corresponding infrared thermal images. e) Normalized integrated spectral intensity variation under continuous 3.0 W (1.18 $W \cdot mm^{-2}$) blue LD irradiation.

As illustrated in Fig. 3a and Fig. S23, the luminescent performance of $SL_{1-x}S_x$: $0.004Eu^{2+}$ ($0 \leq x \leq 0.4$) PCs under blue laser excitation were investigated, using a self-built setup comprising a 450 nm blue LD (with a spot area of 2.543 mm^2), an integrating sphere, a fiber spectrometer, a laser power meter, and an infrared thermal imaging camera. The cut SLS: Eu^{2+} PC rings can be

assembled with high-thermal-conductivity metal substrate and sapphire cover plate as designed for practical application (Fig. S24). With the increased incident laser power (P_{in}) (Fig. 3b), the luminous flux (LF) of $SL_{1-x}S_x$: $0.004Eu^{2+}$ ($0 \leq x \leq 0.4$) PCs initially increases before gradual saturation, with maximum LF of 970.6 lm under laser excitation at a power density of 6.29 W/mm^2 (16 W). Furthermore, even under luminescence saturation, the $SL_{1-x}S_x$: $0.004Eu^{2+}$ ($0 \leq x \leq 0.4$) PCs series exhibits desired red-light conversion efficiency (8.6 %-27.2 %) and excellent red-light color purity (79.8 %-96.5 %) (Fig. 3c). Meanwhile, due to its dense microstructure, the thermal conductivity of the SLS: Eu^{2+} PC reaches 8.16 $W \cdot m^{-1}K^{-1}$ (Table S9). As shown from thermal infrared images, under irradiation by blue laser at a saturated incident power of 16 W (6.29 W mm^{-2}) in rotating mode, the surface temperature of the SLS: Eu^{2+} ceramic wheel is only 96.7 °C (Fig. 3d). Furthermore, the SLS: Eu^{2+} PCs exhibited exceptional resistance to blue LD irradiation, only displaying a slight reduction in red-emission intensity (~2.2 %) after continuous exposure to a 450 nm blue LD (3 W, 1.18 $W \cdot mm^{-2}$) for 120 min (Fig. 3e). This performance is markedly superior to that of pressed SLS: Eu^{2+} powder, $CaAlSiN_3$: Eu^{2+} PC, K_2SiF_6: Mn^{4+} PC, and $CsPb(Br/I)_3$ perovskite glass-ceramics bulk. Moreover, even under substantially higher incident-power-density blue-LD irradiation (15 W, 5.90 $W \cdot mm^{-2}$) for 120 min, the luminescence intensity of SLS: Eu^{2+} PCs could remain ~96.3 % retention, while the spectral features, including the emission peak position and FWHM, were essentially preserved (Fig. S25).

Laser-Driven Lighting and Display

For Review Only

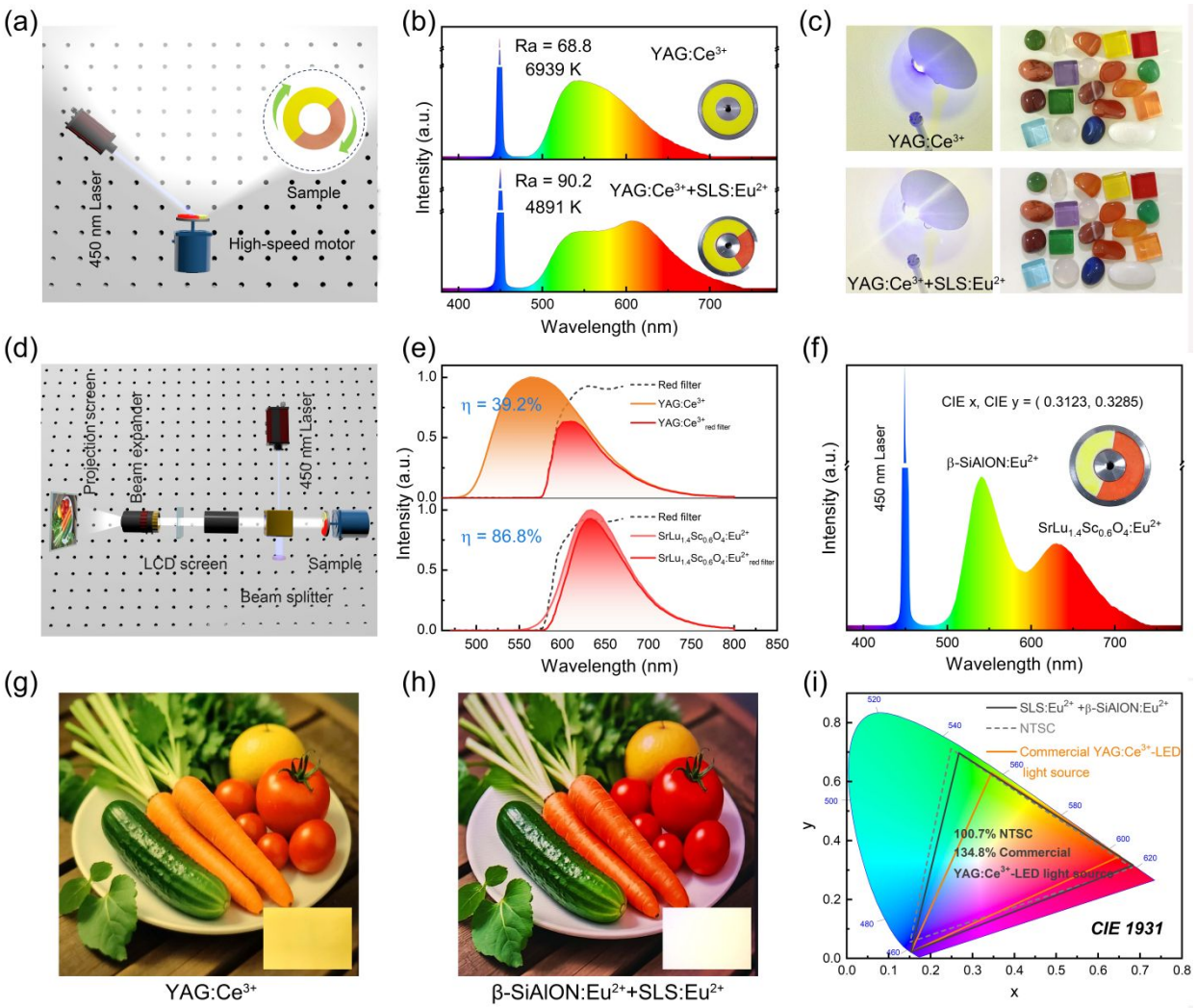


Figure 4 Construction of laser-driven lighting and display systems. (a) Schematic diagram of PC-based laser-driven lighting. (b) Emission spectra of the two fabricated laser-driven lighting. (c) Photographs of objects illuminated under different lighting configurations. (d) Schematic illustration of the optical path in the SLS: Eu^{2+} PC -based laser-driven projection display system. (e) Comparison of the spectra of YAG: Ce^{3+} PC, $SrLu_{1.4}Sc_{0.6}O_4$: Eu^{2+} PC, and the corresponding red emission components extracted using commercial red filter. (f) Emission spectra of the $SrLu_{1.4}Sc_{0.6}O_4$: Eu^{2+} PC-based lighting source for laser-driven projection display prototypes. The display performance of the laser-driven projection display prototypes assembling (g) YAG: Ce^{3+} PC wheel and (h) "β-SiAlON: Eu^{2+} PC + SLS: Eu^{2+} PC" wheel. (i) Corresponding color gamut comparison among the two laser-driven projection display systems and the NTSC standard.

To evaluate its advantages for lighting applications, we fabricated two reflective-type lighting devices, with one relying on conventional YAG: Ce^{3+} PC as the light source and the other adopting

a composite PC system of SLS: Eu^{2+} combined with YAG: Ce^{3+} (Fig. 4a). As shown in Fig. 4b, the spectra indicate that the introduction of SLS: Eu^{2+} PC effectively complements and optimizes the spectral composition in the red region, remarkably reducing the CCT from 6939 K to 4891 K and improving the CRI from Ra = 68.8 to Ra = 90.2 (Notably, the red index R9 is boosted from 38 up to 94.). Correspondingly, the visual color reproduction results directly demonstrate that the "SLS: Eu^{2+} PC + YAG: Ce^{3+} PC" device exhibits distinctly superior lighting quality (Fig. 4c). Additionally, the SLS: Eu^{2+}-based lighting source is also well suited for plant lighting (Fig. S26).

Furthermore, to verify the positive effect of SLS: Eu^{2+} PC in laser-driven display applications, we constructed a display prototype based on "β-SiAlON: Eu^{2+} PC + SLS: Eu^{2+} PC", with the optical path illustrated in Fig. 4d. Spectral variations after filtering by a commercial red filter reveal that the red spectral utilization efficiency of SLS: Eu^{2+} (86.8 %) is 2.2 times that of YAG: Ce^{3+} (39.2 %) (Fig. 4e, S27 and Equation S7). As shown in the spectra (Fig. 4f) and the actual display photographs (Fig. 4g, h), the β-SiAlON: Eu^{2+} + SLS: Eu^{2+} PC-based prototype presents higher color saturation, with more vivid and realistic colors. The β-SiAlON: Eu^{2+} PC + SLS: Eu^{2+} PC-based laser-driven projection display system achieves an exceptionally wide color gamut of 100.7 % NTSC, 134.8 % relative to the YAG: Ce^{3+} PC counterpart (74.7 % NTSC) (Fig. 4i and Table S10). Compared with previously reported Eu^{2+}-activated red-emitting ceramics [11, 12, 30], SLS: Eu^{2+} PCs exhibit unique application potential for laser-driven displays, benefiting from the quantitative modulation of luminescence parameters via tuning Sc doping concentrations (Supplementary Note S1).

CONCLUSIONS

For Review Only

To address the urgent demand for red-emitting materials in laser-driven lighting and displays, SLS: Eu^{2+} solid solution PCs with tunable Sc^{3+} substitution were successfully synthesized as highly dense, transparent, phase-pure red-emitting ceramics. By employing local structure modulation via Lu/Sc substitution to modulate Eu^{2+} luminescence, a tunable emission from 611 to 643 nm was achieved, with a FWHM of 73-83 nm, desired thermal stability (47.3 %@200 °C), high double-85 stability (94.6 %@1200 h), and excellent resistance to blue laser irradiation (96.3 %@120 min, 15 W/5.90 $W \cdot mm^{-2}$). Theoretical and experimental results reveal that Sc substitution effectively modulates the local coordination environment and electronic structure of SLS: Eu^{2+} PCs, synergistically enhancing crystal-field splitting, centroid shift, and bond covalency, and further enabling well-matched blue-LD excitation and tunable deep-red emission. Moreover, SLS: Eu^{2+} PC-based laser-driven prototype lighting sources demonstrate promising application potential for laser-driven lighting and display. The incorporation of SLS: Eu^{2+} PC into YAG: Ce^{3+} PC-based reflective lighting devices effectively supplements the red spectral component, which reduces the CCT, markedly enhances the CRI and R9 value, and enables superior color reproduction. When integrated with a hybrid configuration comprising SLS: Eu^{2+} PC and β-SiAlON: Eu^{2+} PC for laser-driven projection displays, the system delivers substantially more vivid color rendering and a wide color gamut of 100.7 % NTSC.

REFERENCES

1 Ali M, Mohamed M, Chen Y, *et al*. Boosting luminescence in oxide phosphors by the vitrifying-devitrifying approach. Nat Commun, 2026, 17: 6176

2 Wang Y, Li Z, Xue M, *et al*. Recent progress in Eu^{2+} activated red phosphors for white LEDs and laser displays: focusing on efficient host screening and innovative structural design. Coord Chem Rev, 2026, 546: 217060

For Review Only

3 Li C, Liu G, Wang H, *et al*. Laser-driven spinel-type ceramics enabling NIR-II light sources for penetration optical imaging assisted by a guided filter network algorithm. Mater Today, 2025, 91: 196-203

4 Yang Z, Lin S, Zheng S, *et al*. High-efficiency red-emitting phosphor-in-glass films for laser-driven lighting and display. Laser Photonics Rev, 2026, 20: e02185

5 Liu G, Chen W, Xiong Z, *et al*. Laser-driven broadband near-infrared light source with watt-level output. Nat Photonics, 2024, 18: 562-568

6 Cheng Z, Zhou Z, Wang Y, *et al*. Photothermal synergistic AlN-YAG:Ce composite phosphor ceramics for laser-driven lighting applications. J Adv Ceram, 2026, 15: 9221288

7 Zhang H, Zhao J, Yu Z, *et al*. Omnidirectionally encapsulated phosphor-in-glass film converter for laser-driven lighting source. Laser Photonics Rev, 2026, 20: e03165

8 Liu X, Tukachev N, Wang K, *et al*. Hydrogen halide gas sensors: active materials, operation principles, and emerging technologies. Interdiscip Mater, 2026, 5: 85-123

9 Wang G, Xiong W, Qiu L, *et al*. Second-level fast sintering enables high-brightness light source for visible light communication. Nat Commun, 2026, 17: 7973

10 Xi G, Lin S, Shen T, *et al*. Transparent ceramic@sapphire composites for high-power laser-driven lighting. Adv Sci, 2025, 12: 2505232

11 Yang Z, de Boer T, Braun P, *et al*. Thermally stable red-emitting oxide ceramics for laser lighting. Adv Mater, 2023, 35: 2301837

12 Tian R, Wang Q, Li S, *et al*. Efficient $Sr_{0.5}Ca_{0.5}AlSiN_3:Eu^{2+}$ red-emitting ceramics for high-power solid-state lighting. J Mater Sci Technol, 2025, 210: 179-187

13 Gu S, Yang Z, Lian H, *et al*. High-performance $(Y_{1-x}Ce_x)_3Al_5O_{12}$ ceramics synthesized by spark plasma sintering for high-power laser-driven lighting. J Rare Earths, 2026, 44: 67-74

14 Lai Y, Zheng J, Zhang Z, *et al*. Core-cladding-like phosphor ceramic wafer: a path to ultrahigh luminance. J Adv Ceram, 2025, 14: 9221137

15 Zhang X, He M, Li P, *et al*. Hierarchical ceramic encapsulation strategy enables robust perovskite nanocrystals for next-generation laser-driven diodes. Laser Photonics Rev, 2026, 20: e01789

16 Chen G, Li S, Zhou W, *et al*. Interface reaction inhibition in phosphor-in-silica glass for high-performance laser illumination. Sci China Mater, 2026, 69: 4568-4577

For Review Only

17 Wang P, Lin H, Chen G, *et al*. Rapid sintering of high-efficiency phosphor-in-glass films for laser-driven light source. Nat Commun, 2025, 16: 2807

18 Zhuo S, Lin S, Pang T, *et al*. Transparent ceramic-quantum dots glass film composites with high-efficiency thermal management for laser-driven projection display. Adv Funct Mater, 2026, 36: e16371

19 Zhu S, Jin S, Zhan L, *et al*. Glass network engineering of yellow-emitting $Ba_2Sc_2B_4O_{11}:Ce^{3+}$ glass ceramics for full-spectrum lighting. J Adv Ceram, 2025, 14: 9221169

20 Hu Y, Qiao J, Li D, *et al*. Recent developments in near-infrared phosphors for broad-band light-emitting diodes light sources. J Rare Earths, 2026, 44: 1625-1645

21 de Wit J, van Swieten T, van de Haar M, *et al*. Increasing the power: absorption bleach, thermal quenching, and auger quenching of the red-emitting phosphor $K_2TiF_6:Mn^{4+}$. Adv Opt Mater, 2023, 11: 2202974

22 Pan Z, Zhuo S, Qin Z, *et al*. Ultra-stable $CsPbBr_3@Y_2O_3$ translucent ceramic with a record-high thermal conductivity for laser-driven applications. Adv Funct Mater, 2025, 35: 2509643

23 Zhang M, Dong X, Yue D, *et al*. Large-sized $K_2SiF_6:Mn^{4+}$ phosphor crystals up to 3 mm grown by seeded growth with near-unity quantum efficiency. J Alloys Compd, 2026, 1053: 186239

24 Pang T, Lin S, You F, *et al*. Synergistic enhancement of crystallinity and transparency in Tb^{3+}-doped nano-glass-ceramics for high-resolution X-ray imaging. J Adv Ceram, 2025, 14: 9221122

25 Hu T, Guo Y, Yi X, *et al*. Integrated multi-responsive $SrMg_2Al_6Si_9O_{30}:Eu^{2+}$ osumilite glass ceramic via in situ crystallization: a unified platform for smart optical applications. Adv Funct Mater, 2026, 36: e31457

26 Wang M, Zhou X, Li Q, *et al*. Recent advances in CPL-active chiral materials: from organic/metal complexes to stimuli-responsive regulation. Interdiscip Mater, 2026, 5: 357-377

27 Lin S, Zhang Y, Gu R, *et al*. Ultra-high-crystallinity transparent glass-ceramic scintillators for high-temperature X-ray imaging. Sci China Mater, 2026, https://doi.org/10.1007/s40843-026-4315-2

For Review Only

28 Zhang L, Qiao J, Wang L, *et al*. Unlocks photoluminescence quantum efficiency enhancement in Eu^{2+}-doped phosphors via bond angle variance index. Angew Chem Int Ed, 2025, 64: e202515249

29 Chen W, Wang Y, Liu G, *et al*. Si/Al order and texture orientation optimization of red-emitting $Mg_2Al_4Si_5O_{18}:Eu^{2+}$ ceramics for laser phosphor display. J Materiomics, 2024, 10: 1137-1143

30 Chen W, Wang Y, Xu J, *et al*. Red-emitting cordierite ceramic enabling general healthy warm white laser lighting. Laser Photonics Rev, 2024, 18: 2300963

31 Kim K, Kang E, Kang B, *et al*. Synthesis of $SrLu_2O_4:Eu^{2+}$ red phosphors and their photoluminescence properties. J Lumin, 2017, 183: 13-16.

32 Zhao J, Sun X, Wang Z. Ce^{3+}/Eu^{2+} doped $SrSc_2O_4$ phosphors: synthesis, luminescence and energy transfer from Ce^{3+} to Eu^{2+}. Chem Phys Lett, 2018, 691: 68-72

33 Richards R, Ciobanu C. Can Hume-Rothery rules predict single-phase high-entropy rocksalt oxide phases? Philos Mag Lett, 2024, 104: 2433726

34 Wang S, You F, Wang S, *et al*. Deep-red $(Sr,Ba)Lu_2O_4$: Eu^{2+} phosphor for full-spectrum lighting. Phys Status Solidi-R, 2024, 18: 2400061

35 Yang Z, Zhao Y, Zhou Y, *et al*. Giant red-shifted emission in $(Sr,Ba)Y_2O_4:Eu^{2+}$ phosphor toward broadband near-infrared luminescence. Adv Funct Mater, 2022, 32: 2103927

36 Hu T, Gao Y, Molokeev M, *et al*. Eu^{2+} stabilized at octahedrally coordinated Ln^{3+} site enabling red emission in $Sr_3LnAl_2O_{7.5}$ (Ln = Y or Lu) phosphors. Adv Opt Mater, 2021, 9: 2100077

37 Li G, Wang Y, Guo H, *et al*. Electronic structure, photoluminescence and phosphorescence properties in $BaSc_2Si_3O_{10}:Eu^{2+}$, RE^{3+} (RE^{3+} = Nd^{3+}, Tm^{3+}, Dy^{3+} and Tb^{3+}) phosphors. J Lumin, 2017, 192: 98-104

38 Tian R, Zhou T, Xie R. Spectrally tunable dual-phosphor ceramics for laser lighting. Laser Photonics Rev, 2025, 19: 2402144

39 Tian R, Li S, Zhou T, *et al*. Laser-driven dual-ceramic converters enabling high-luminance white light. Ceram Int, 2025, 51: 60577-60582

For Review Only

40 Wang P, Wang Y, Li Z, *et al*. Enhanced stability and brightness through Co-substitution: promoting plant growth with green-excited deep red phosphor $Ca_{1-z}Sr_zLi_{1-x}Mg_{2x}Al_{3-x}N_4:yEu^{2+}$. Adv Mater, 2025, 37: 2414578

41 Wang X, Qu J, Zhang H, *et al*. A reflective sapphire@PiGF@alumina color converter enabling ultrahigh luminescence laser-driven white lighting. J Adv Ceram, 2025, 14: 9221124

42 Dou C, Song Z, Liu Q. Progress of Ce^{3+}/Eu^{2+} doped phosphors for violet chip based full-spectra lighting. J Mater Chem C, 2024, 12: 11209-11241

43 Jin J, Han K, Wang Y, *et al*. Bandgap narrowing in europium(II)-based bromide hybrids toward improved X-ray scintillation and imaging. Chem Mater, 2024, 36: 4813-4820

44 Dorenbos P. 5d-level energies of Ce^{3+} and the crystalline environment. III. Oxides containing ionic complexes. Phys Rev B, 2001, 64: 125117

45 Kuang Y, Chen W, Wang Y, *et al*. Narrow-band green/red-emitting glass composites enabling highly stable patterned wheel for laser phosphor display. Sci China Mater, 2025, 68: 1822-1829

46 Zhou Y, Ji R, Su Z, *et al*. Breaking concentration quenching for excellent highly efficient and stable narrowband luminescence by structural ordering and defect regulation. Rare Met, 2026, 45: e70087

47 Yu H, Qin L, Wang X, *et al*. Development of Eu^{2+}-doped UCr_4C_4-type phosphors toward advanced display applications. Laser Photonics Rev, 2025, 19: e00740

48 Tian R, Zhou T, Xie R. Laser-driven composite ceramic enabling superhigh-luminance white light. J Materiomics, 2025, 11: 101059

49 Wu Y, Li X, Ruan C, *et al*. Tough transparent glass ceramics for multi-mode programmable dynamic tunable persistent luminescence via phase engineering. Nat Commun, 2026, 17: 3267

50 Lin J, Chen S, Ye W, *et al*. Ultra-stable yellow monolithic perovskite quantum dots film for backlit display. Adv Funct Mater, 2024, 34: 2314795

51 Hu D, Lin S, Pang T, *et al*. Ultra-narrowband green-emitting transparent composite ceramics for laser-driven display. Adv Mater, 2025, 37: 2414957

Acknowledgement

For Review Only

This research was supported by National Natural Science Foundation of China (52572155, 12304442 and 52272141), Natural Science Foundation of Fujian Province (2024J02014 and 2024J01949), and Natural Science Foundation of Fujian for Excellent Young Scholars (2026J009042).

Author contributions

Chen D and Lin S supervised the research. Hu D synthesized the material and wrote the first draft. Lin S and Chen D helped Hu D to analyze the experimental results and finish the final manuscript. Zheng Y, Zeng L, Li X, Huang F, and Xie A provided constructive suggestions for data analyses. Li X, An R, Xie R, Zhou Z, and Chen B helped to measure the spectroscopy. Li X and Zheng Y helped to make a computational procedure. All authors agreed on its final content.

Conflict of interest

The authors declare that they have no conflict of interest.

Supplementary information

Supplementary materials are available in the online version of the paper.



Dahai Hu is currently a doctoral student in Prof. Daqin Chen's research group at Fujian Normal University. His current research focuses on ceramics-based luminescent materials.



For Review Only

Shisheng Lin is an associate professor at the College of Physics and Energy, Fujian Normal University. He received his Ph.D. degree from the Fujian Institute of Research on the Structure of Matter, Chinese Academy of Sciences, in 2021. His research mainly focuses on the photofunctional glass ceramics/ceramics, as well as their applications.



Xiaoyan Li is a full professor at the College of Electronics and Information Science, Fujian Jiangxia University. She received his Ph.D. degree from the Fujian Normal University, in 2020. Her research mainly focuses on the optoelectronic functional glass ceramics and devices.



Daqin Chen is a full professor at the College of Physics and Energy, Fujian Normal University. He received his Ph.D. degree from the Fujian Institute of Research on the Structure of Matter, Chinese Academy of Sciences, in 2008. His research mainly focuses on the design, synthesis, and applications of advanced luminescent materials, including rare-earth-doped nanomaterials, transparent glass ceramics, and perovskite quantum dots, as well as their applications in optoelectronic devices.

For Review Only

用于激光照明和显示的新型红光 $Sr(Lu, Sc)_2O_4$: Eu^{2+}透明陶瓷

胡大海 [1], 林世盛 [1*], 郑勇平 [1], 曾令玮 [2], 安然 [1], 谢榕 [1], 周哲泓 [1], 陈彬 [1], 李小燕 [3*], 黄烽 [1], 谢安 [4], 陈大钦 [1,5*]

摘要 高效、稳定的红光荧光陶瓷是先进光电器件领域亟需的关键材料。本研究成功制备了一系列具有红光发射特性的 $Sr(Lu_{1-x}Sc_x)_2O_4$: Eu^{2+} (SLS: Eu^{2+})固溶体陶瓷。该系列陶瓷展现出优异的红光发射性能（611-643 nm，半峰宽 73-83 nm）、良好的热稳定性（47.3 %@200 ℃）

及卓越的双 85 稳定性（1200 h 后为 94.6 %），同时具备出色的高功率蓝光激光辐照耐受能力（15 W、5.90 W mm^{-2} 条件下 96.3 %@120 min）。理论计算与实验结果共同揭示，Sc^{3+} 部分取代 Lu^{3+}引起[Sc/Lu/EuO_6]八面体收缩及晶格畸变加剧，并增强 Eu-O 键的共价性，从而协同实现发射光谱的精准调控与材料性能的优化。此外，基于 SLS: Eu^{2+}荧光陶瓷分别构建了激光驱动照明与显示原型器件。其中，照明原型器件可产生色温为 4891 K、显色指数高达 90.2 的中性白光；显示原型器件则可实现超过 100 % NTSC 的宽色域显示。本研究为面向激光驱动照明与显示技术的高性能红色发光材料设计提供了新的研究思路。

For Review Only

Supporting Information

Novel Red-Emitting $Sr(Lu, Sc)_2O_4$: Eu^{2+} Transparent Ceramics for Laser-Driven Lighting and Display

Dahai Hu[1], Shisheng Lin[1*], Yongping Zheng[1], Lingwei Zeng[2], Ran An[1], Rong Xie[1], Zhehong Zhou[1], Bin Chen[1], Xiaoyan Li[3*], Feng Huang[1], An Xie[4], Daqin Chen[1,5*]

[1]College of Physics and Energy, Fujian Provincial Key Laboratory of Quantum Manipulation and New Energy Materials, Fujian Normal University, Fuzhou, Fujian, 350117, P. R. China

[2]School of Chemistry and Chemical Engineering, Key Laboratory of Theoretical Organic Chemistry and Functional Molecule of Ministry of Education, Hunan University of Science and Technology, Xiangtan, Hunan, 411201, P. R. China

[3]College of Electronics and Information Science, Fujian Jiangxia University, Fuzhou, Fujian, 350108, P. R. China

[4]School of Materials Science and Engineering, Key Laboratory of Functional Materials and Applications of Fujian Province, Xiamen University of Technology, Xiamen, Fujian, 361024, P. R. China

[5]Fujian Provincial Engineering Technology Research Center of Solar Energy Conversion and Energy Storage, Fuzhou, Fujian, 350117, P. R. China

*Corresponding author (email: linshisheng@fjnu.edu.cn; xyli@fjjxu.edu.cn; dqchen@fjnu.edu.cn)

For Review Only

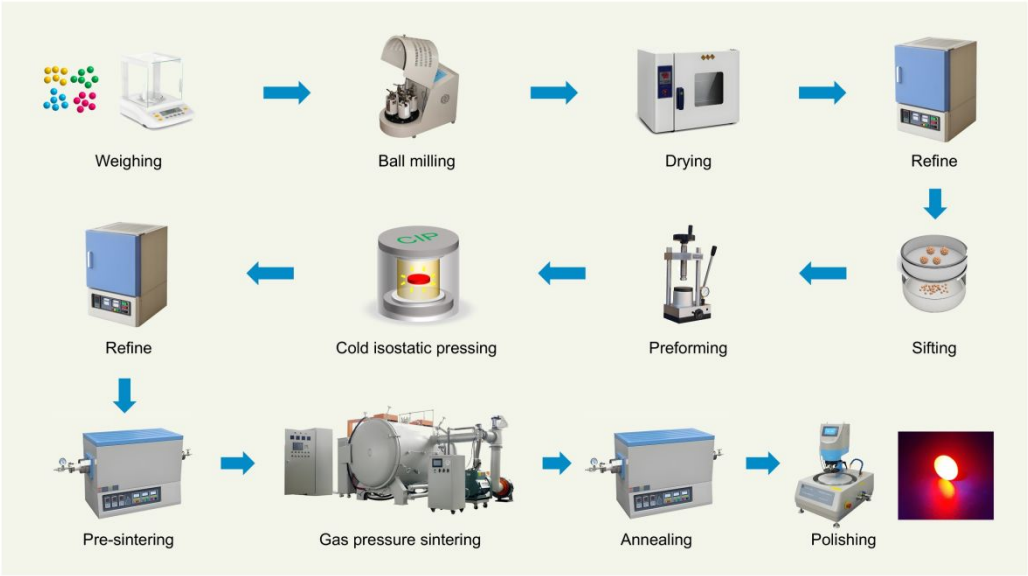


Figure S1. Schematic diagram of preparation process of $Sr(Lu_{1-x}Sc_x)_2O_4$: Eu^{2+} phosphor ceramics (SLS: Eu^{2+} PCs).

For Review Only

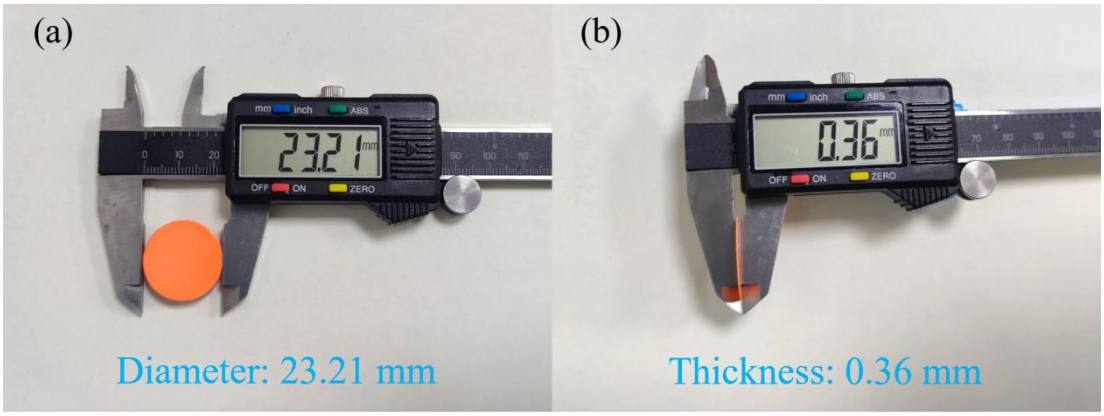


Figure S2. Diameter and thickness of SLS: Eu^{2+} ceramic sample.

For Review Only

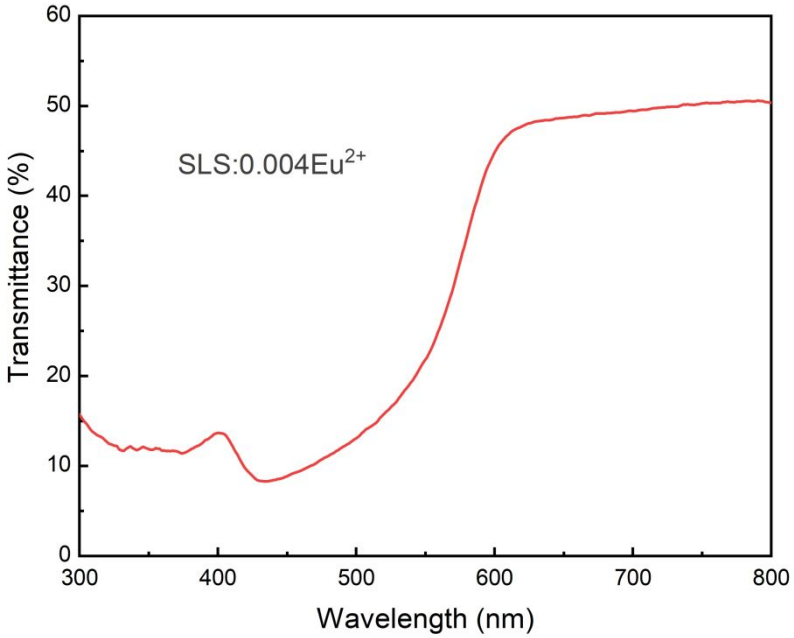


Figure S3. Transmittance spectra of SLS: 0.004Eu^{2+} ceramic.

For Review Only

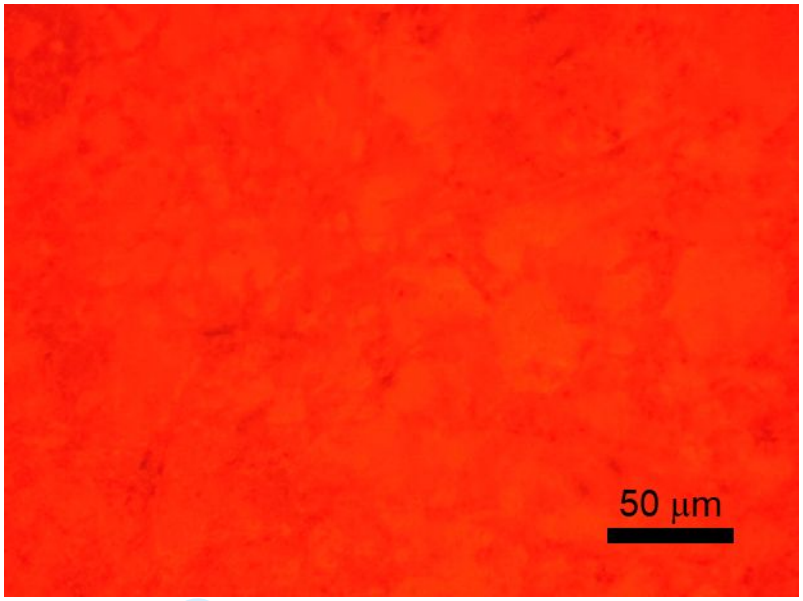


Figure S4. Fluorescence microscopy image of the SLS: $0.004Eu^{2+}$ ceramic under 450 nm excitation.

For Review Only

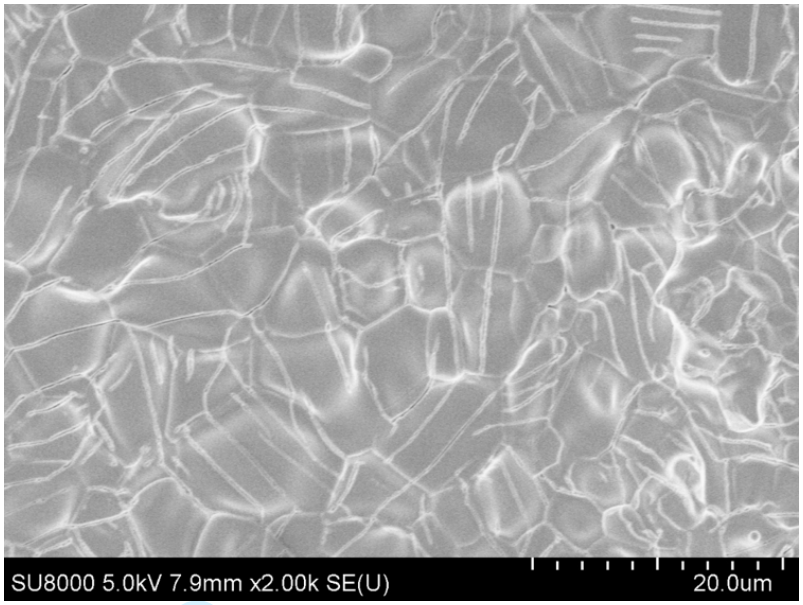


Figure S5. SEM images of SLS: 0.004Eu^{2+} ceramic.

For Review Only

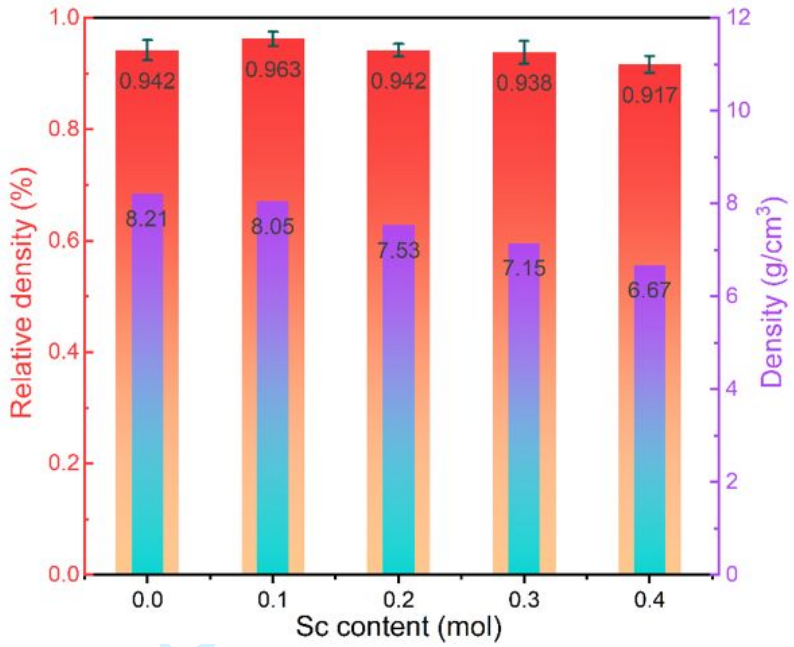


Figure S6. The relative density and density of $Sr(Lu_{1-x}Sc_x)_2O_4$: $0.004Eu^{2+}$ ($0 \leq x \leq 0.4$) PCs.

For Review Only

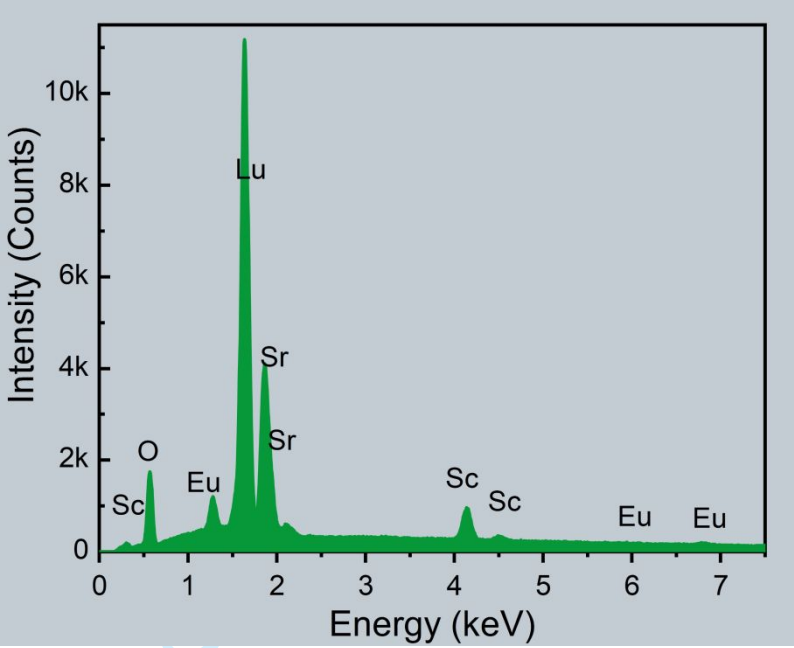


Figure S7. EDS spectrum of SLS: $0.004Eu^{2+}$ ceramic.

For Review Only

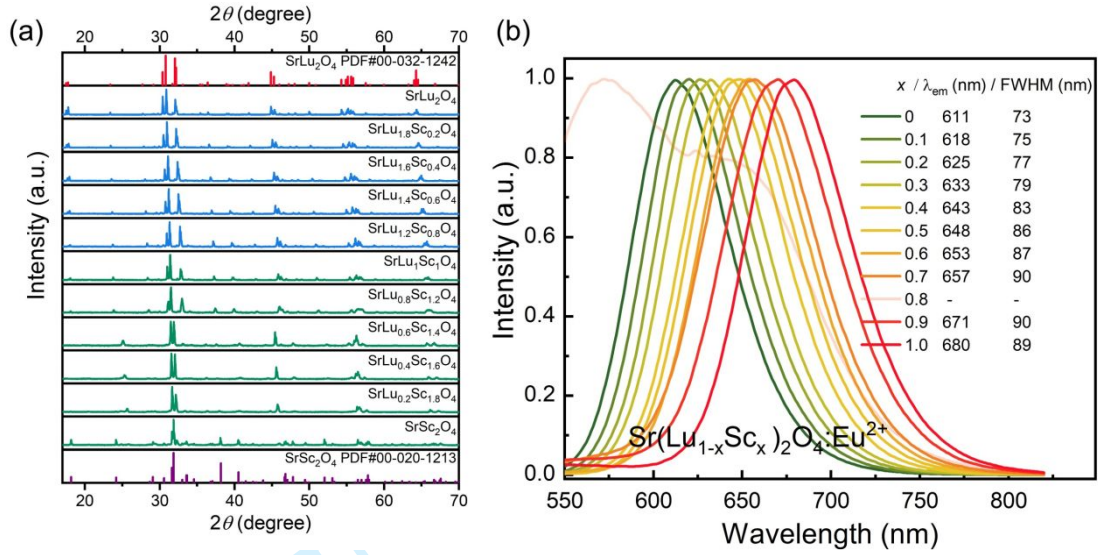


Figure S8. (a) XRD patterns and (b) PL spectra of samples with increasing Sc ($0 \leq x \leq 1$) doping concentration.

Discussions on Figure S8:

Sc doping of the system was performed over the entire concentration range, and the XRD data are shown in Figure S8. Once the Sc doping level is above x = 0.6, the $SrLu_2O_4$ host phase is no longer detectable, with abundant impurities emerging. The underlying origin lies in the 15.6% ionic radius discrepancy between six-coordinated Sc^{3+} ($R_{CN\ =\ 6}$ = 0.745 Å) and Lu^{3+} ($R_{CN\ =\ 6}$ = 0.861 Å) [1]. Constrained by the Hume-Rothery rules [2], the $Sr(Lu_{1-x}Sc_x)_2O_4$: Eu^{2+} ($0 \leq x \leq 1$) system tends to form a limited solid solution, and full-range infinite mutual solubility cannot be achieved.

Comprehensively considering phase purity, the human visual efficiency for red light energy (<650 nm), and the CIE-specified red spectral band for display applications (630-650 nm), we chose the Sc doping range of $0 \leq x \leq 0.4$ for this study. $Sr(Lu_{1-x}Sc_x)_2O_4$: Eu^{2+} maintains the single-phase $SrLu_2O_4$ crystal structure at low Sc substitution levels ($0 \leq x \leq 0.4$).

For Review Only

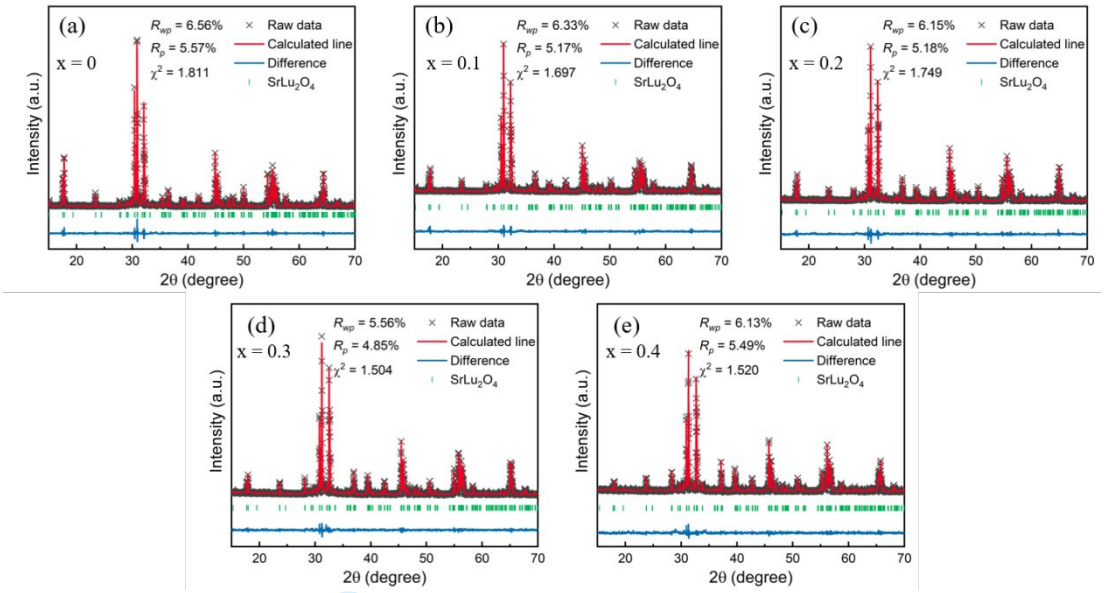


Figure S9. Rietveld refinement XRD patterns of $Sr(Lu_{1-x}Sc_x)_2O_4$: $0.004Eu^{2+}$ ($0 \leq x \leq 0.4$) PCs.

For Review Only

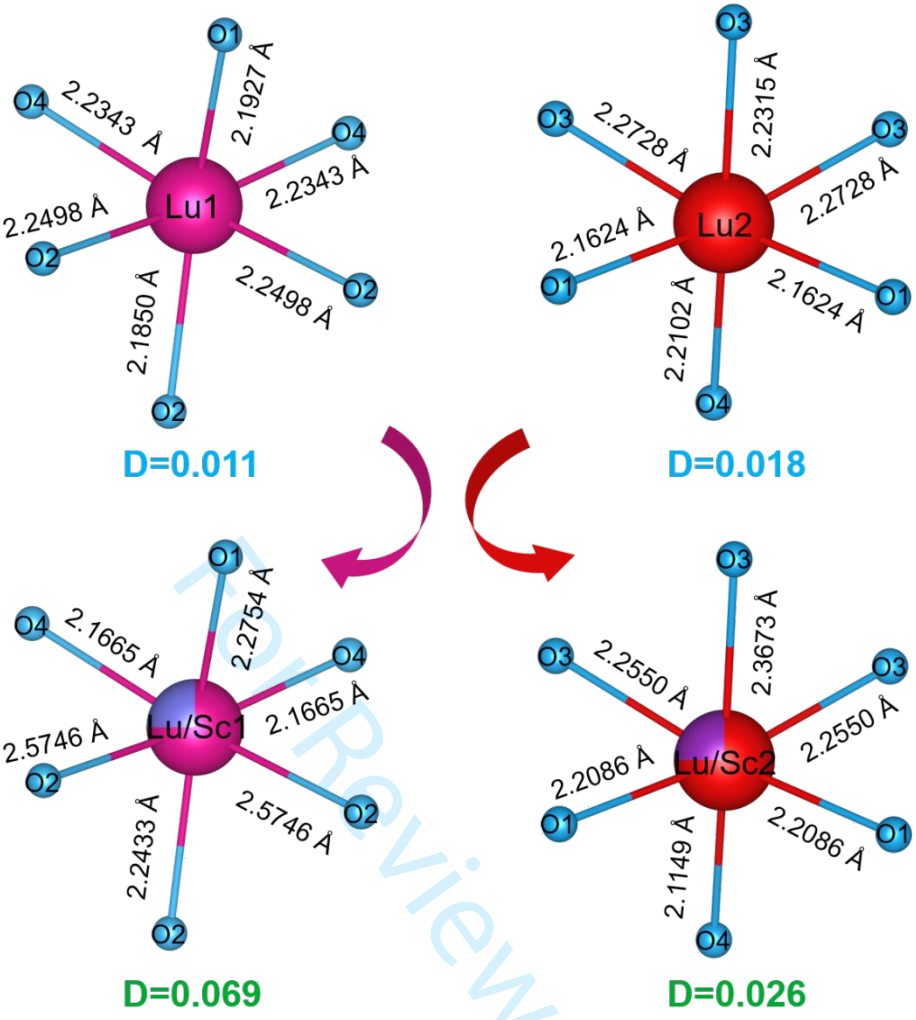


Figure S10. The local coordination structure of the Lu1/Lu2 sites.

Discussions on Figure S10:

In order to further explore the influence of the coordinated polyhedron, distortion index (D) also be calculated [3]:

$$D = \frac{1}{n}\sum_{i=1}^{n}\frac{|R_i - R_{av}|}{R_{av}} \qquad \text{(Equation S1)}$$

where n is the coordination number, R_i is the bond length between cation and coordinated anions, and R_{av} is the average bond length.

For Review Only

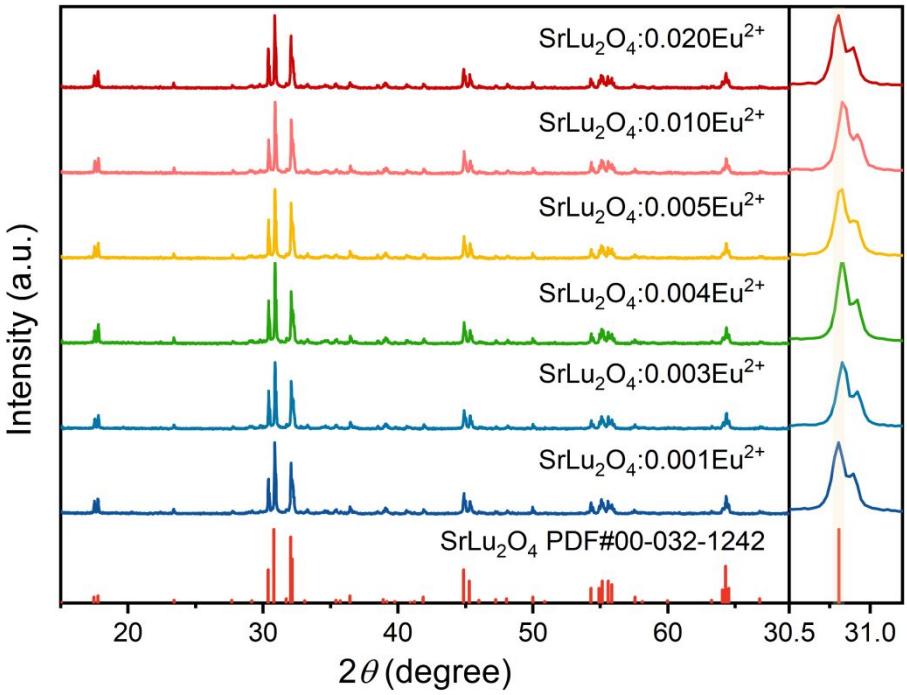


Figure S11. XRD patterns of $SrLu_2O_4$: yEu^{2+} ($0.001 \leq y \leq 0.02$) PCs.

Review Only

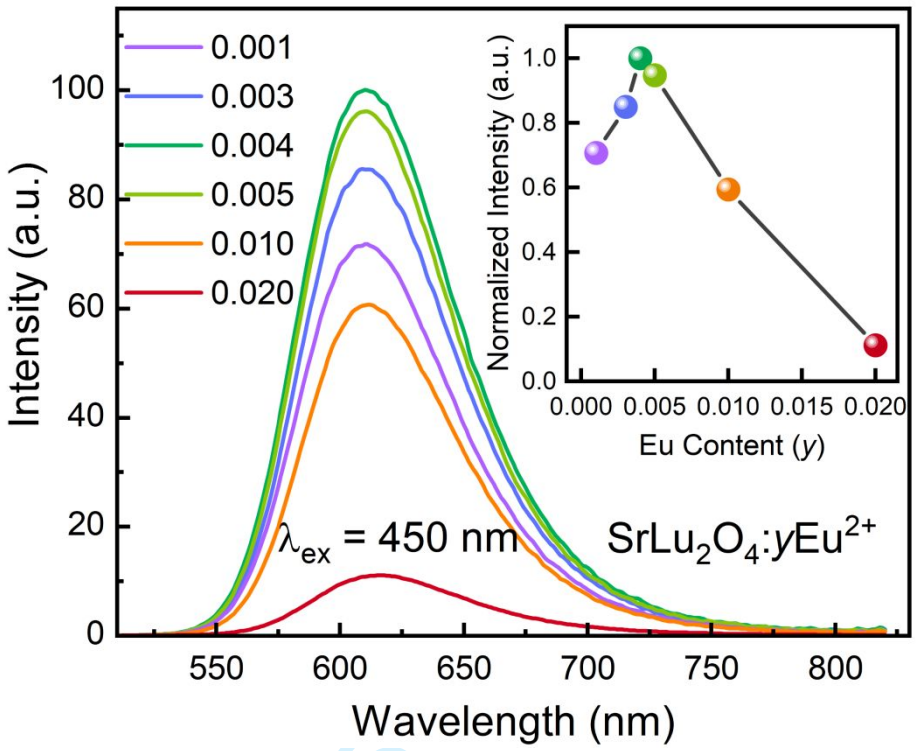


Figure S12. PL spectra of $SrLu_2O_4$: yEu^{2+} ($0.001 \leq y \leq 0.02$), the inset shows Eu^{2+} content-dependent PL intensity.

For Review Only

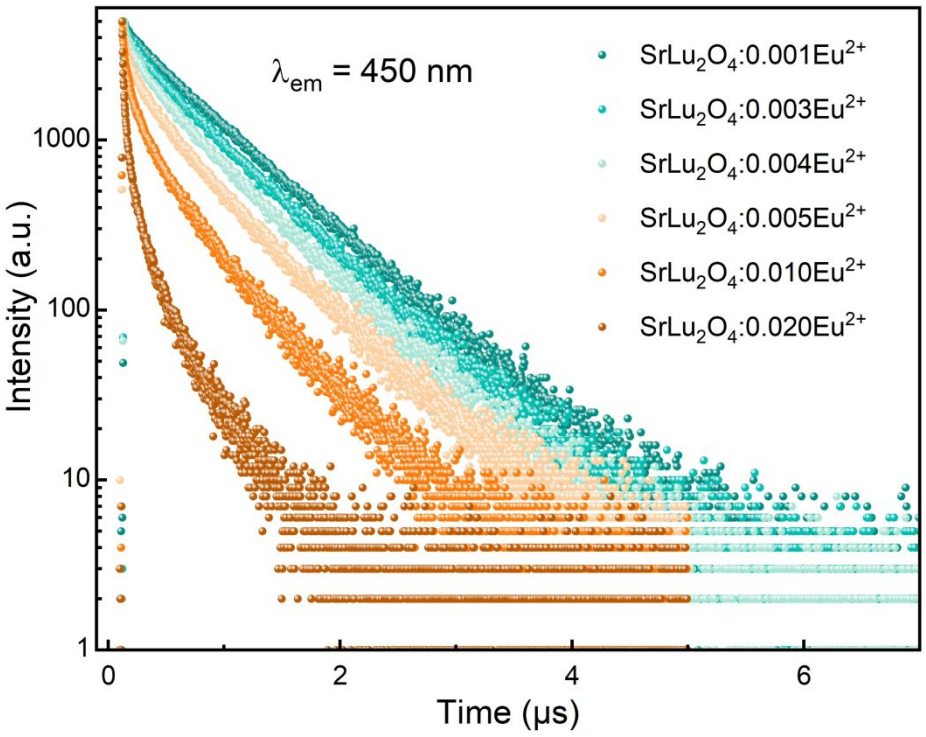


Figure S13. Luminescent decay curves of $SrLu_2O_4$: yEu^{2+} ($0.001 \leq y \leq 0.02$) PCs.

Discussions on Figure S13:

The luminescence decay curve of SLS: Eu^{2+} ceramics could be well-fitted as follows equation [4]:

$$I(t) = A\exp(-t/\tau_1) + B\exp(-t/\tau_2) \qquad \text{(Equation S2)}$$

where I(t) represent the luminescence intensity at the time t, A and B are the corresponding fitted decay constants, and τ_1 and τ_2 stand for the lifetimes for exponential components.

Review Only

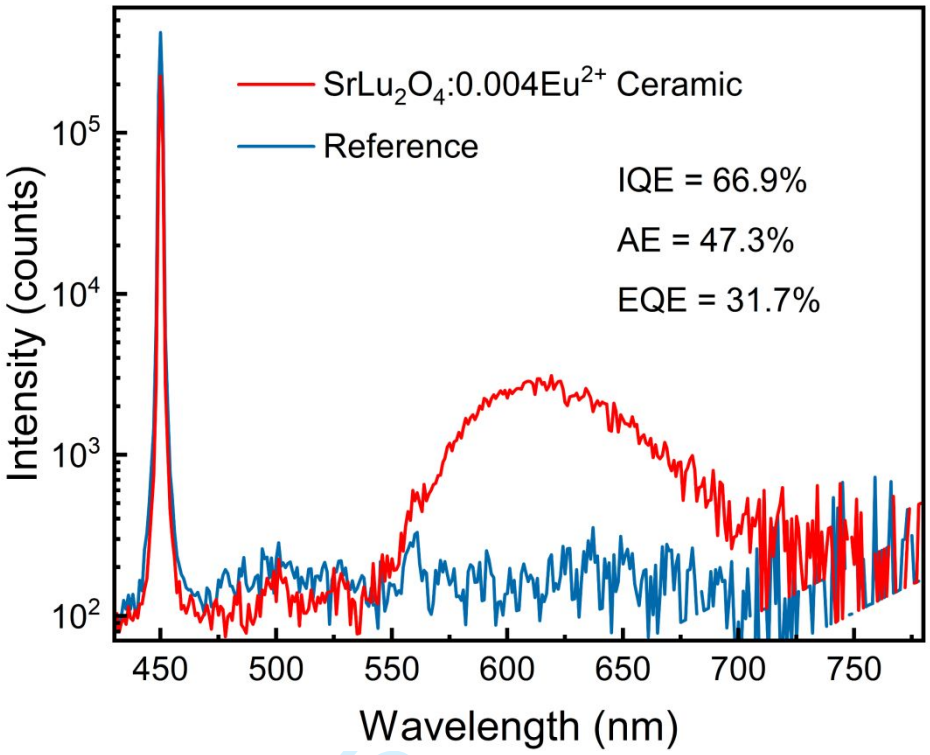


Figure S14. The EQE, IQE, and AE for $SrLu_2O_4$: $0.004Eu^{2+}$ PC under 450 nm.

Discussions on Figure S14:

The internal quantum efficiency (IQE), absorption efficiency (AE) and external quantum efficiency (EQE) can be calculated by the following equation [5]:

$$IQE = \frac{AEM_{emission}}{AEX_{reference} - AEX_{sample}} \quad \text{(Equation S3)}$$

$$AE = \frac{AEX_{reference} - AEX_{sample}}{AEX_{reference}} \quad \text{(Equation S4)}$$

$$EQE = IQE \times AE \quad \text{(Equation S5)}$$

where $AEM_{emission}$ denotes the integration area of the emission spectrum, and $AEX_{reference}$ and AEX_{sample} denote the integration area of the excitation spectrum without and with the sample on the integrating sphere, respectively. Herein, polytetrafluoroethylene is used as the reference.

Review Only

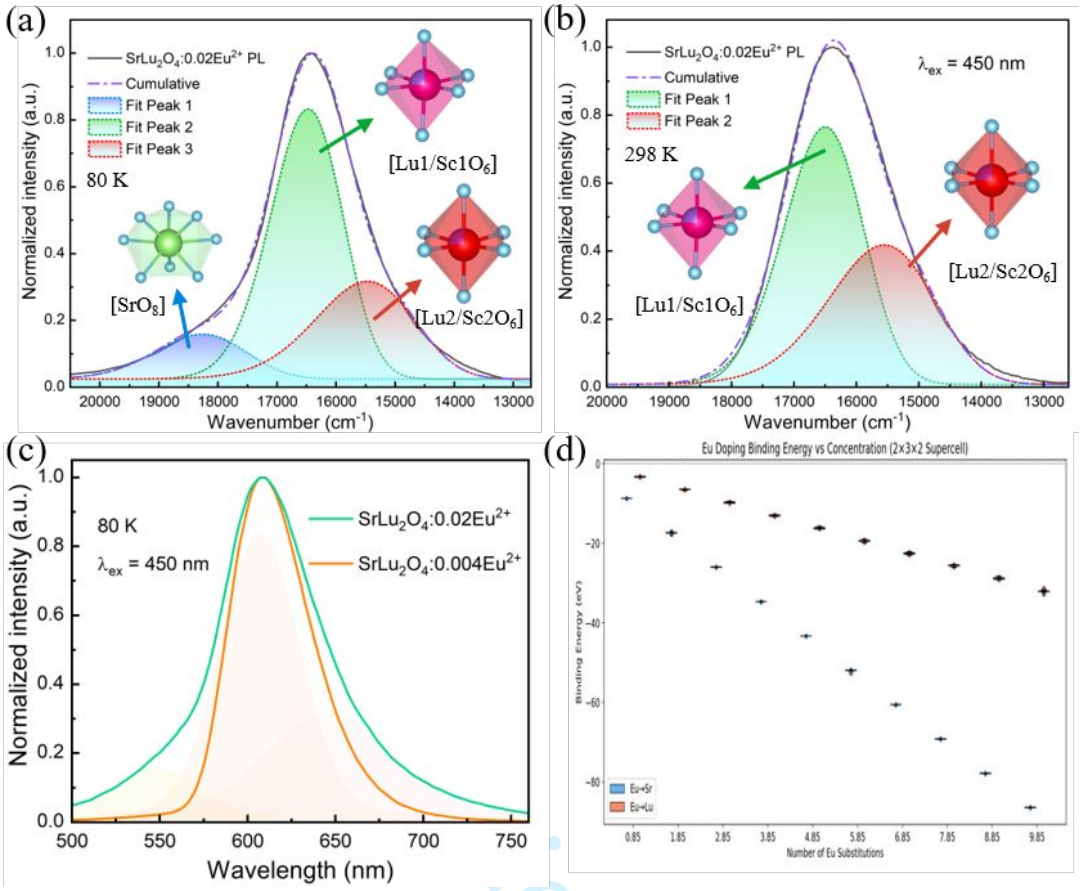


Figure S15. Gaussian fitting curves of $SrLu_2O_4$: $0.02Eu^{2+}$ ceramics measured at (a) 80K and (b) 298K. (c) PL spectra of $SrLu_2O_4$: yEu^{2+} (y = 0.004 and 0.02) measured at 80K. (d) The dopant formation energies of Eu^{2+} substituting the sites in $SrLu_2O_4$ models.

Discussions on Figure S15:

The PL spectra of $SrLu_2O_4$: $0.02Eu^{2+}$ measured at 80 K indicate that at high Eu doping content, Eu^{2+} substitutes for the Sr^{2+} site and two Lu^{3+} sites (formation energy of Lu1 site < Lu2 site). In addition, thermal broadening and emission thermal quenching impair radiative luminescence and thereby alter spectral distribution, rendering the Eu^{2+} emission from Sr sites nearly negligible at room temperature [6, 7]. At low Eu doping content, the emission band of $SrLu_2O_4$: $0.004Eu^{2+}$ can be well deconvoluted into two Gaussian peaks [4, 5], where the more intense Eu1(Lu1) emission peak is located at 16486 cm^{-1} (606 nm) and the weaker Eu2(Lu2) emission peak is located at 15550 cm^{-1} (643 nm). Formation energy calculations indicate only minor differences between Sr and Lu substitution sites at low doping concentrations, consistent with and corroborating the experimental results [8, 9].

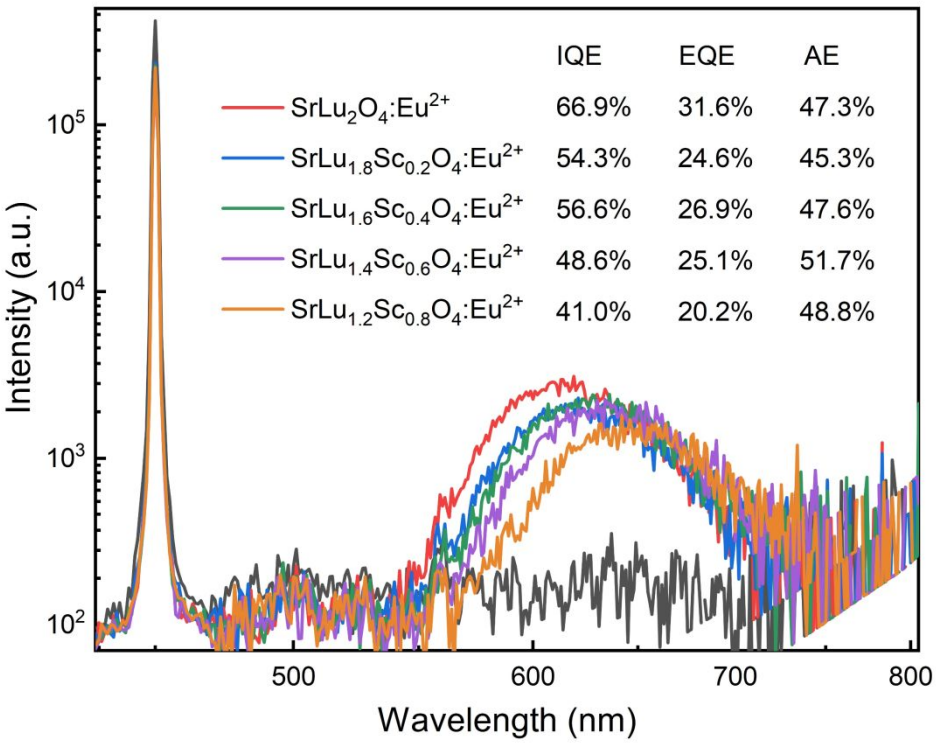


Figure S16. The EQEs, IQEs, and AEs for $Sr(Lu_{1-x}Sc_x)_2O_4$: $0.004Eu^{2+}$ ($0 \leq x \leq 0.4$) PCs under 450 nm.

Review Only

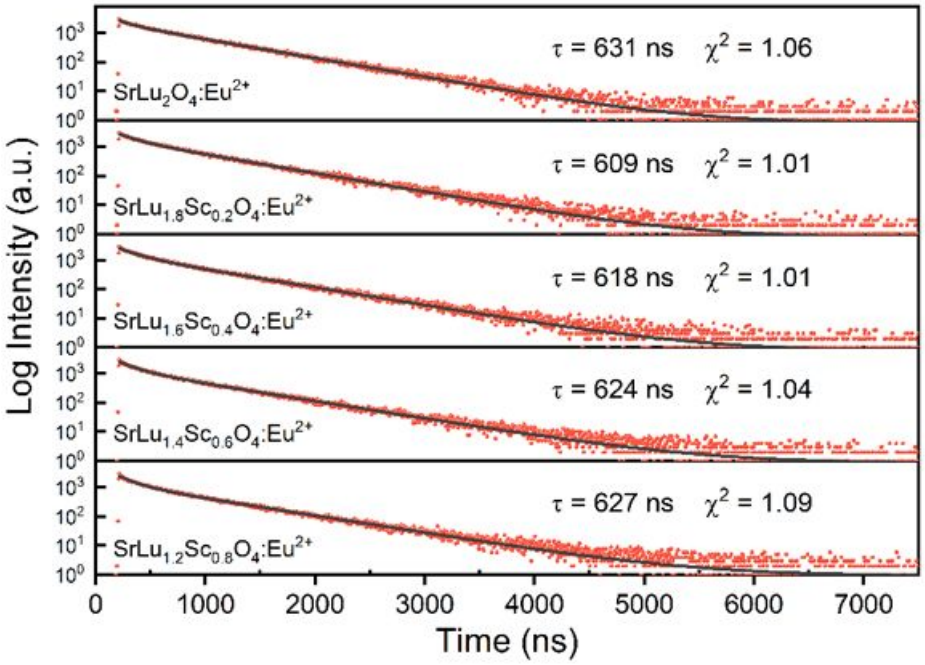


Figure S17. Luminescent decay curves of $Sr(Lu_{1-x}Sc_x)_2O_4$: $0.004Eu^{2+}$ ($0 \leq x \leq 0.4$) PCs.

For Review Only

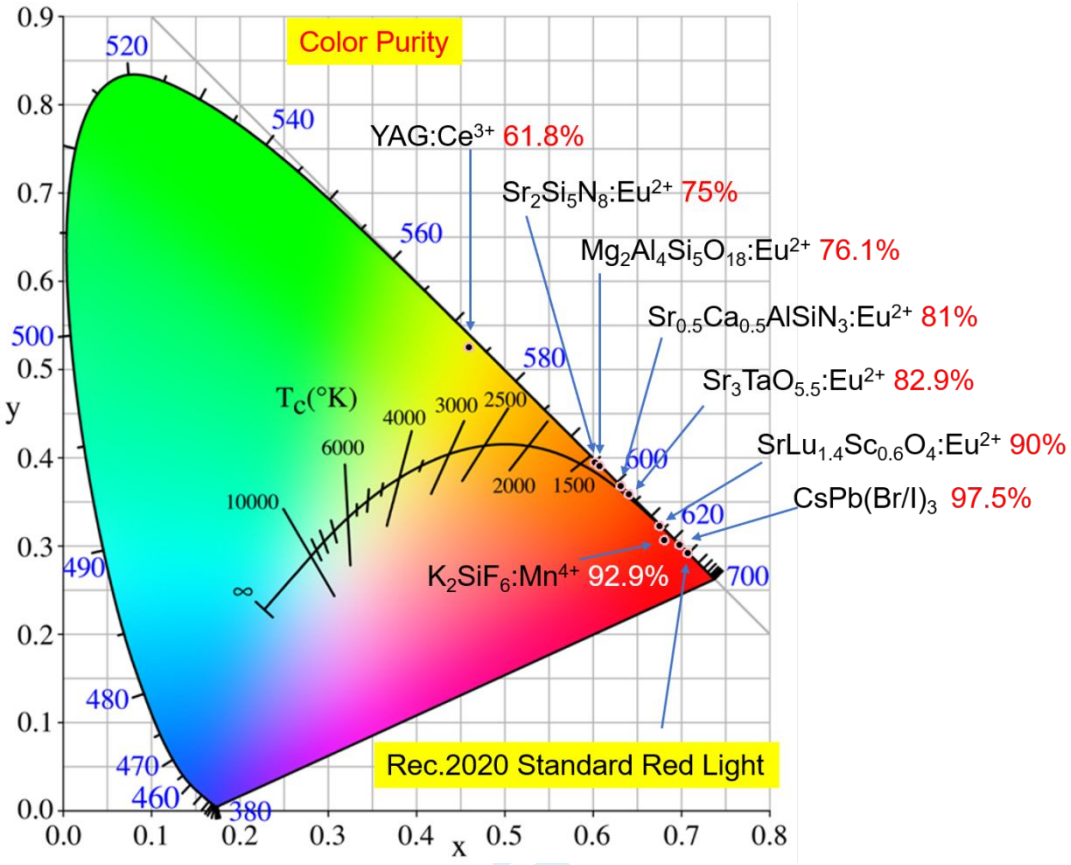


Figure S18. Color purity of SLS: Eu^{2+} ceramic and typical red luminescent materials.

Discussions on Figure S18:

The color purity is an important parameter for red emitter, which can be evaluated asing the following formula [10]:

$$Color\ purity = \frac{\sqrt{(x-x_w)^2+(y-y_w)^2}}{\sqrt{(x_r-x_w)^2+(y_r-y_w)^2}} \times 100\% \qquad \text{(Equation S6)}$$

where (x, y), (x_w, y_w), and (x_r, y_r) are the color coordinates of the samples, white light, and the corresponding dominant red light, respectively. Here, the chromaticity coordinate of white light and dominant red light are based on Rec.2020 standard, which are (0.3127,0.3290) and (0.708,0.292), respectively.

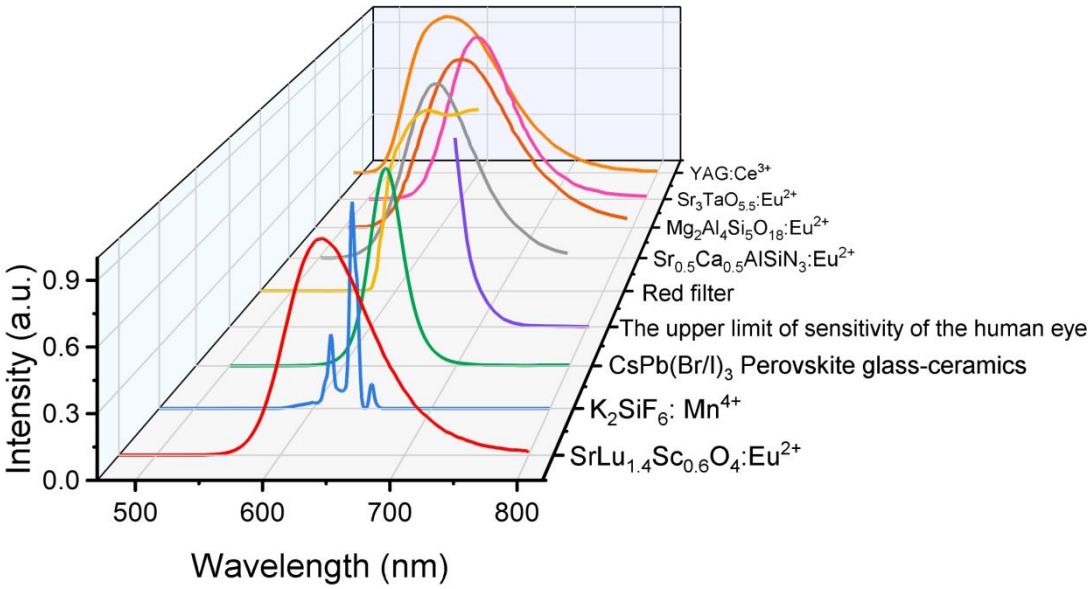


Figure S19. PL spectra of SLS: Eu^{2+} ceramic and typical red luminescent materials.

For Review Only

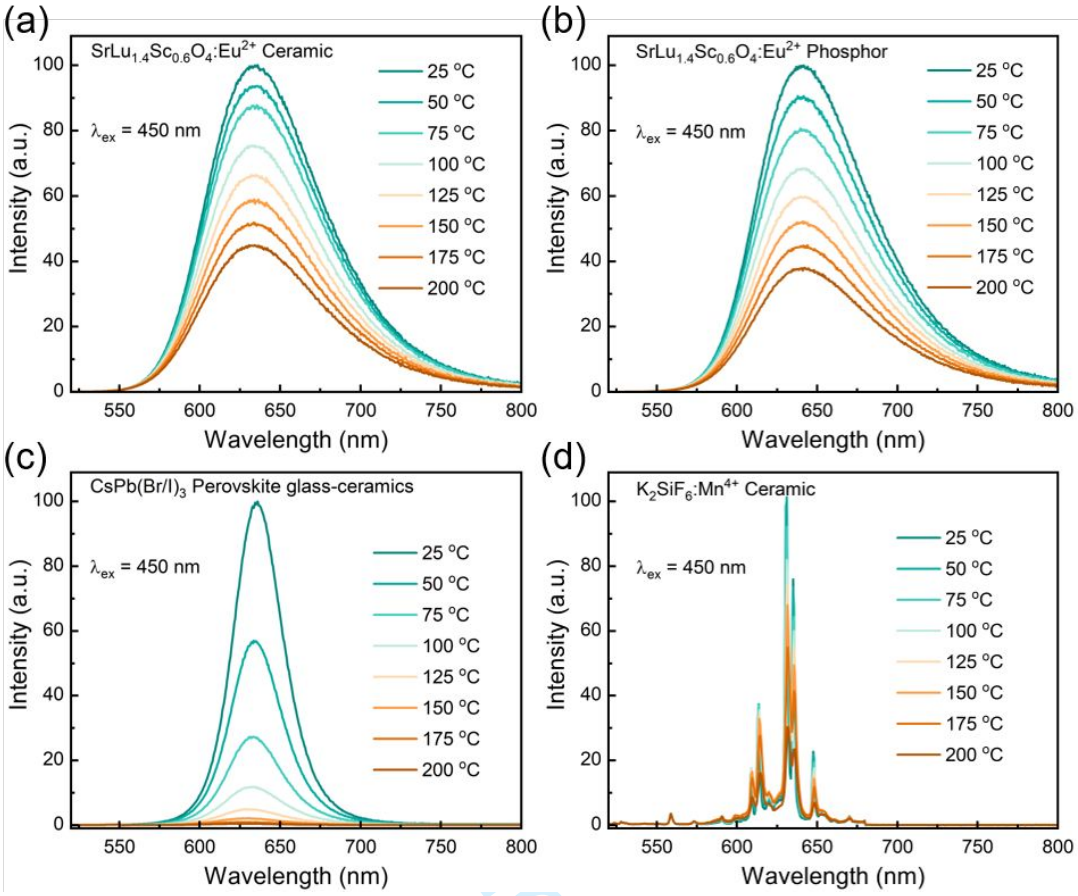


Figure S20. Temperature-dependent PL spectra of (a) SLS: $0.004Eu^{2+}$ ceramic and (b) phosphor, (c) $CsPb(Br/I)_3$ perovskite glass-ceramics, and (d) K_2SiF_6: Mn^{4+} ceramic from room temperature to 200 ℃.

For Review Only

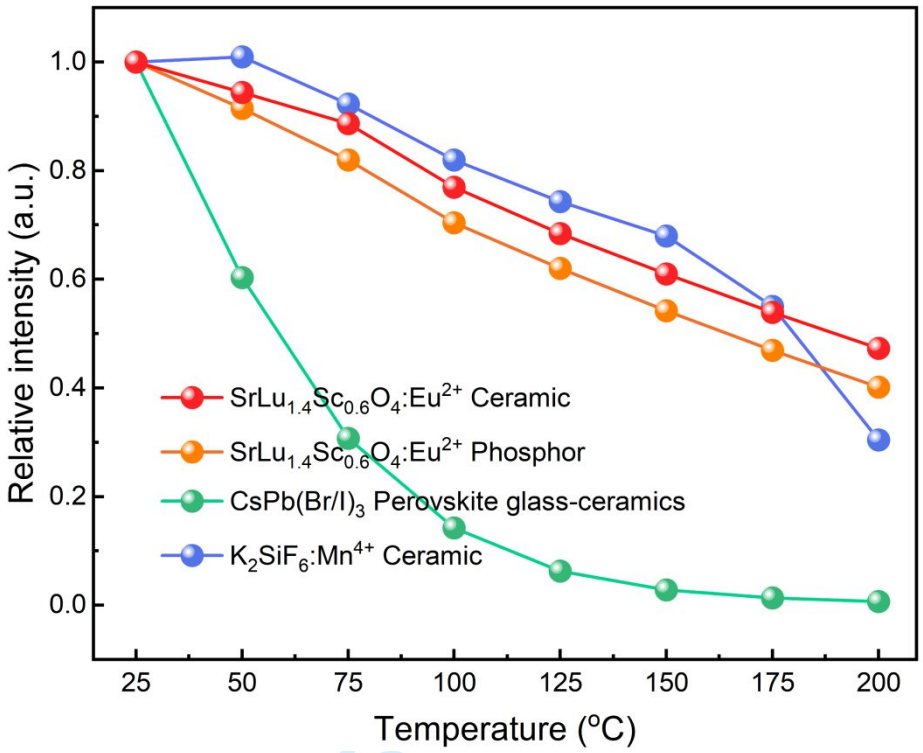


Figure S21. Relative integrated intensity of PL spectra SLS: $0.004Eu^{2+}$ ceramic and phosphor, $CsPb(Br/I)_3$ perovskite glass-ceramics, and K_2SiF_6: Mn^{4+} ceramic at different temperatures, respectively.

For Review Only

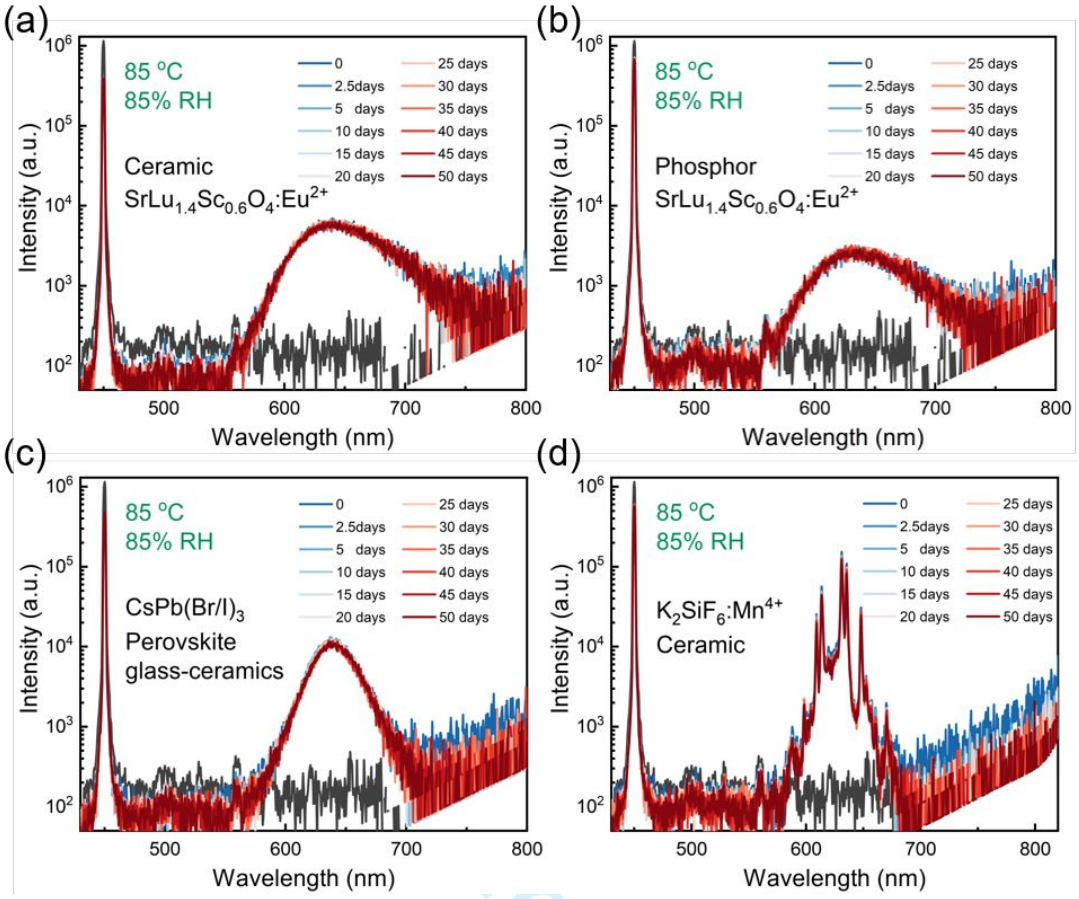


Figure S22. PL spectra of (a) SLS: 0.004Eu^{2+} ceramic and (b) phosphor, (c) $CsPb(Br/I)_3$ perovskite glass-ceramics, and (d) K_2SiF_6: Mn^{4+} ceramic under accelerated aging condition at 85 °C/85 %RH.

For Review Only

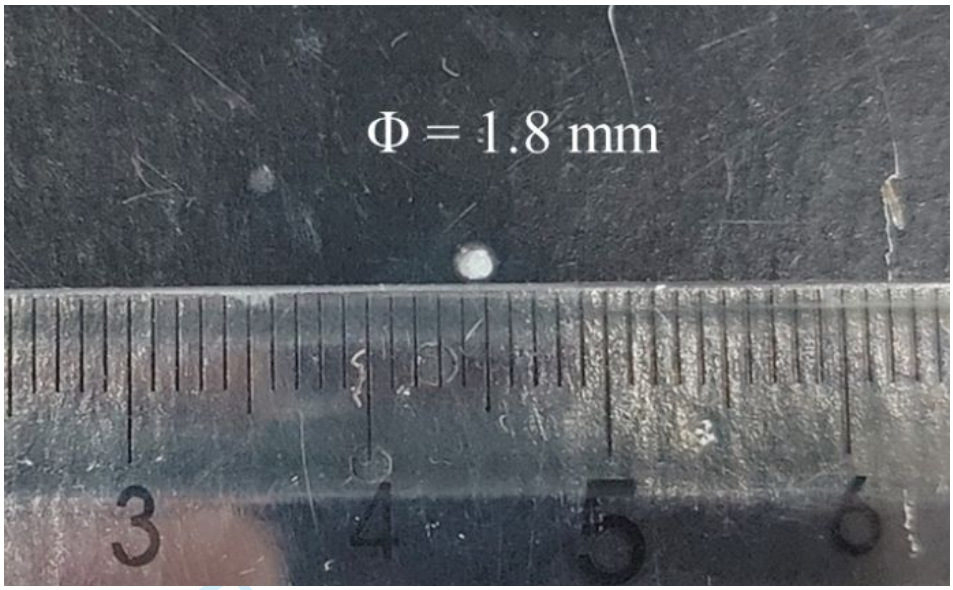


Figure S23. Spot size of 450 nm laser measured by photosensitive paper.

For Review Only

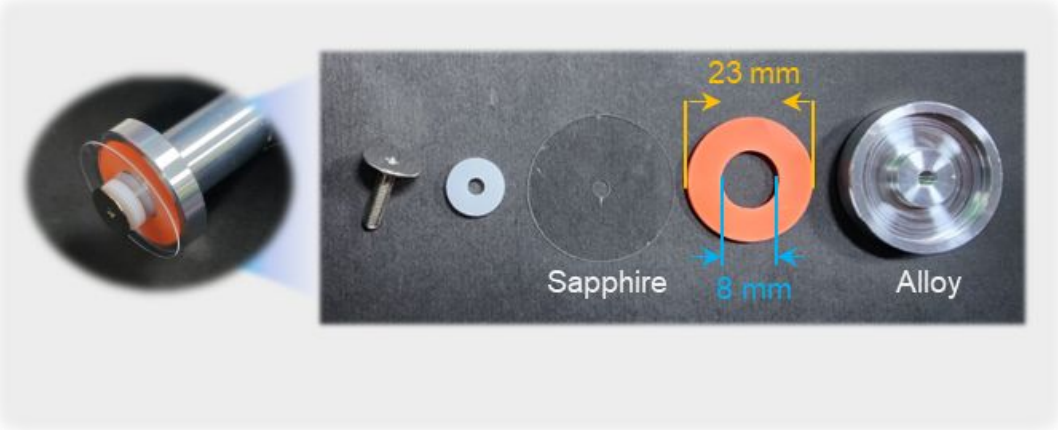


Figure S24. Schematic diagram of sample assembly and ceramic dimensions.

Discussions on Figure S24:

All ceramic samples were subjected to post-treatments including polishing, grinding, and drilling to fabricate ceramic rings with designed dimensions ($\Phi_{external}$ = 23 mm, $\Phi_{internal}$ = 8 mm). These ceramic rings can be further conveniently assembled with high-thermal-conductivity metal substrates and sapphire cover plates for application. This confirms that the ceramics exhibit significantly superior processability and convenience over conventional phosphors.

For Review Only

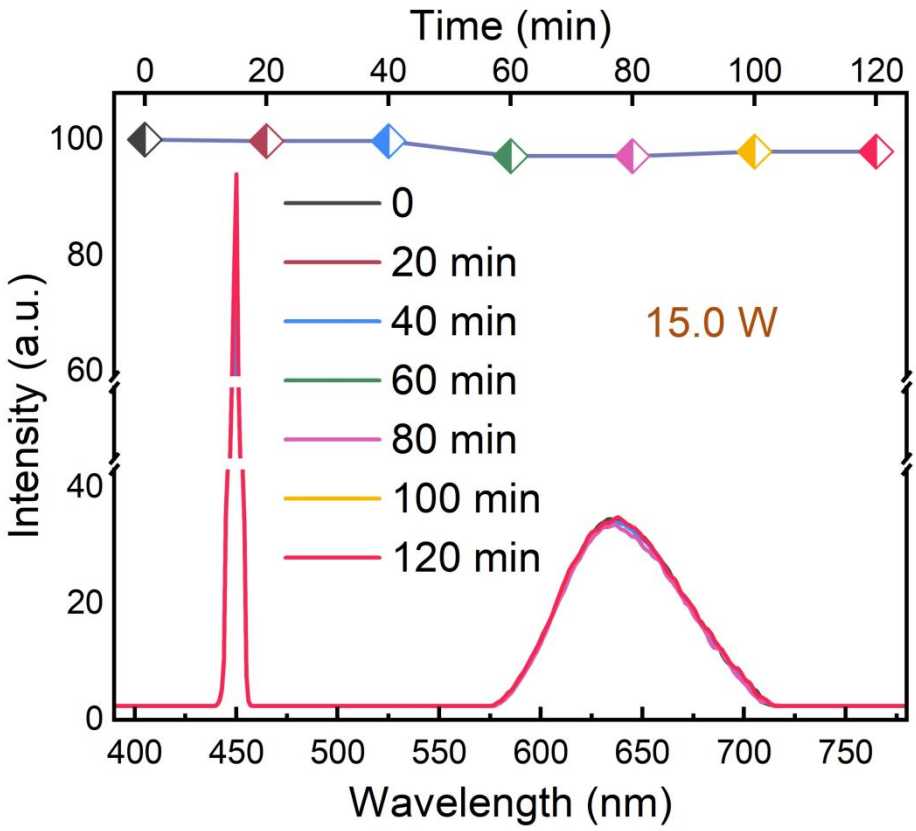


Figure S25. EL spectra of SLS: $0.004Eu^{2+}$ ceramic upon 15W laser irradiation for 120 min.

View Only

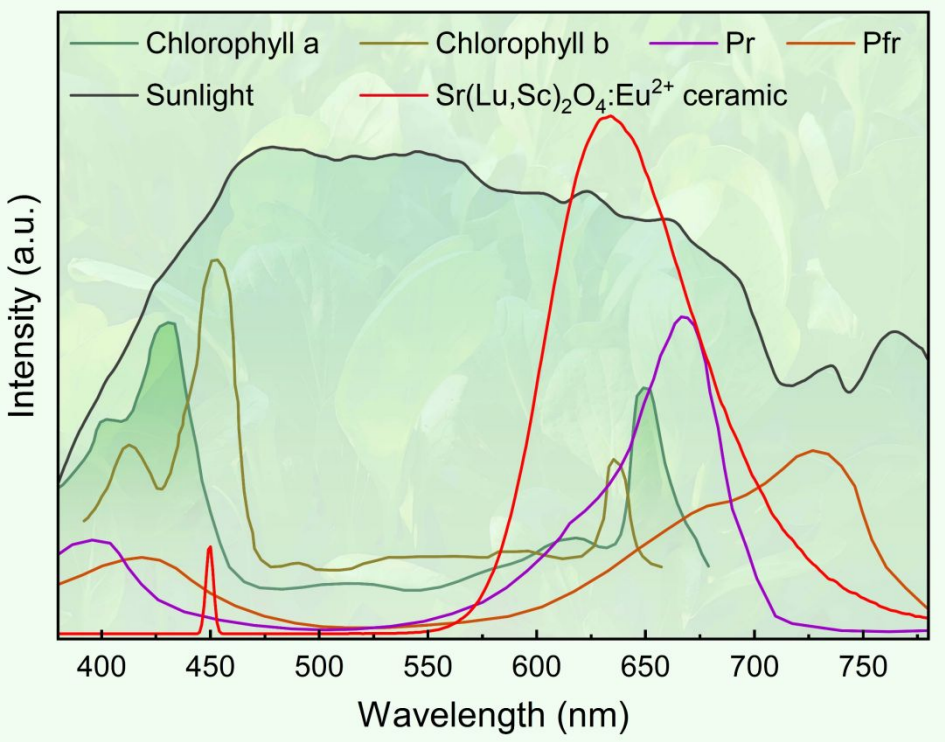


Figure S26. Normalized absorption spectra of plant pigments and EL spectrum of SLS: Eu^{2+} ceramic.

Discussions on Figure S26:

The emission band of SLS: Eu^{2+} ceramic overlaps significantly with the absorption bands of plant pigments, particularly Pr and chlorophyll b. Such spectral matching effectively boosts photosynthesis, modulates plant growth rate and regulates plant morphogenesis.

Review Only

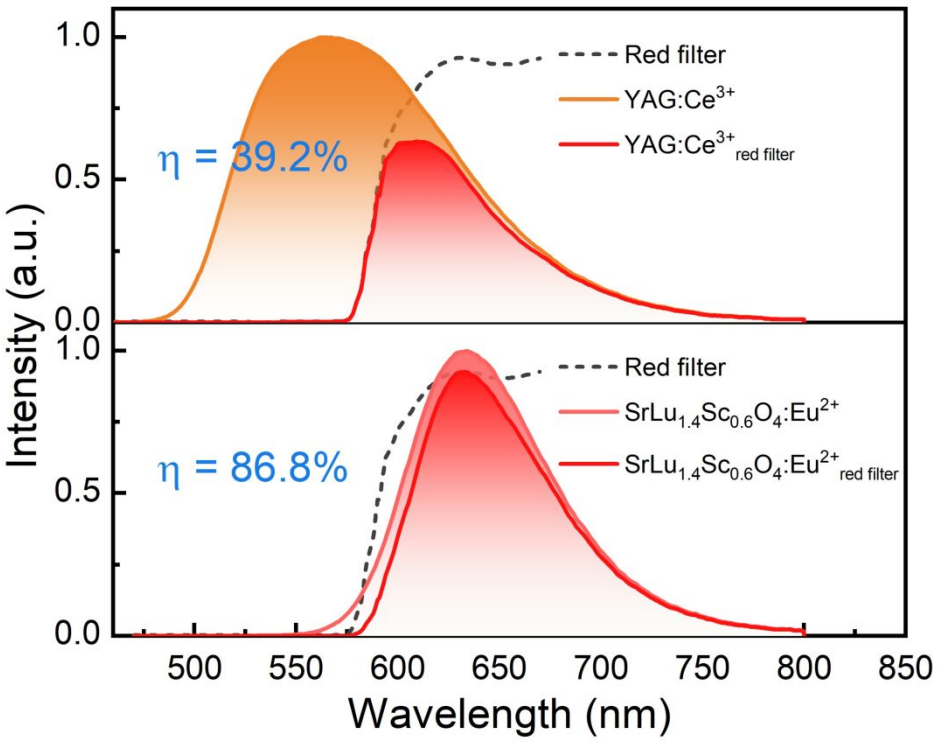


Figure S27. PL spectra of YAG: Ce^{3+} and $SrLu_{1.4}Sc_{0.6}O_4$: Eu^{2+} PC and their red spectrum produced by the commercial red filter.

Discussions on Figure S27:

The spectral utilization efficiency after passing through the commercial red filter can be calculated by integrating the spectral area [11]:

$$\eta = S_{After\ filtration} / S_{Before\ filtration} \qquad \text{(Equation S7)}$$

where, η stands for spectral utilization, $S_{After\ filtration}$ represents the integral intensity of the filtered spectrum, and $S_{Before\ filtration}$ represents the initial emission spectral integral intensity of the PC wheel.

Review Only

Table S1. The color gamut of laser-driven displays and the related optical parameters of red-ceramic converters.

Red ceramics	λ_{ex} [nm]	λ_{em} [nm]	FWHM (nm)	Ra	Color gamut [% NTSC]	Refs.
$Sr_3TaO_{5.5}$: Eu^{2+}	450	620	73	90	-	[12]
$Mg_2Al_4Si_5O_{18}$: Eu^{2+}	450	625	103	85.9	83.4	[11, 13]
$Sr_{0.5}Ca_{0.5}AlSiN_3$: Eu^{2+}	-	625	83	-	-	[14]
$Sr(Lu_{1-x}Sc_x)_2O_4$: Eu^{2+}	450	611-643	73-83	90.2	100.7	This work

For Review Only

Table S2. Refined crystallographic parameters of $Sr(Lu_{1-x}Sc_x)_2O_4$: $0.004Eu^{2+}$ PCs.

Empirical formula	$SrLu_2O_4$: $0.004Eu^{2+}$	$SrLu_{1.8}Sc_{0.2}O_4$: $0.004Eu^{2+}$	$SrLu_{1.6}Sc_{0.4}O_4$: $0.004Eu^{2+}$	$SrLu_{1.4}Sc_{0.6}O_4$: $0.004Eu^{2+}$	$SrLu_{1.2}Sc_{0.8}O_4$: $0.004Eu^{2+}$
Crystal system	orthorhombic	orthorhombic	orthorhombic	orthorhombic	orthorhombic
Space group	P n m a (No.62)	P n m a (No.62)	P n m a (No.62)	P n m a (No.62)	P n m a (No.62)
Formula units (unit cell)	4	4	4	4	4
a (Å)	9.9788(1)	9.9497(1)	9.9187(1)	9.8885(1)	9.8433(2)
b (Å)	3.3431(0)	3.3268(0)	3.3119(0)	3.2969(0)	3.2731(0)
c (Å)	11.7545(1)	11.7118(1)	11.6671(1)	11.6225(1)	11.5532(2)
α (°)	90	90	90	90	90
β (°)	90	90	90	90	90
γ (°)	90	90	90	90	90
Volume (Å^3)	391.89(1)	387.67(1)	383.26(1)	378.91(1)	372.22(1)
R_{wp} (%)	6.56	6.33	6.15	5.56	6.13
R_p (%)	5.57	5.17	5.18	4.85	5.49
χ^2	1.811	1.697	1.749	1.504	1.520

For Review Only

Table S3. The atomic coordinates, occupancy and isotropic thermal displacement parameters (Å^2) of $SrLu_2O_4$: 0.004Eu^{2+} ceramic.

Atom	Wyck.	S.O.F.	x	y	z	U (Å^2)
Sr1	4c	1	0.24902	1/4	0.6443	0.0034
Lu1	4c	0.9972	0.08056	1/4	0.38809	0.0078
Lu2	4c	0.9988	0.57382	1/4	0.61296	0.0078
Eu1	4c	0.0028	0.08056	1/4	0.38809	0.0078
Eu2	4c	0.0012	0.57382	1/4	0.61296	0.0078
O1	4c	1	0.07788	1/4	0.05898	0.0021
O2	4c	1	0.3041	1/4	0.29791	0.0030
O3	4c	1	0.35531	1/4	0.01324	0.2685
O4	4c	1	0.47053	1/4	0.80851	0.0839

For Review Only

Table S4. The atomic coordinates, occupancy and isotropic thermal displacement parameters (Å^2) of $SrLu_{1.8}Sc_{0.2}O_4$: $0.004Eu^{2+}$ ceramic.

Atom	Wyck.	S.O.F.	x	y	z	U (Å^2)
Sr1	4c	1	0.24783	1/4	0.64438	0.0005
Lu1	4c	0.8772	0.07967	1/4	0.3884	0.0077
Lu2	4c	0.9188	0.57422	1/4	0.61264	0.0076
Sc1	4c	0.12	0.07967	1/4	0.3884	0.0077
Sc2	4c	0.08	0.57422	1/4	0.61264	0.0076
Eu1	4c	0.0028	0.0796	1/4	0.3884	0.0077
Eu2	4c	0.0012	0.57422	1/4	0.61264	0.0076
O1	4c	1	0.07521	1/4	0.06017	0.0125
O2	4c	1	0.29866	1/4	0.30796	0.0247
O3	4c	1	0.36638	1/4	0.03102	0.2557
O4	4c	1	0.48986	1/4	0.80384	0.0825

For Review Only

Table S5. The atomic coordinates, occupancy and isotropic thermal displacement parameters (Å^2) of $SrLu_{1.6}Sc_{0.4}O_4$: $0.004Eu^{2+}$ ceramic.

Atom	Wyck.	S.O.F.	x	y	z	U (Å^2)
Sr1	4c	1	0.24712	1/4	0.64566	0.0008
Lu1	4c	0.7376	0.07993	1/4	0.38793	0.0073
Lu2	4c	0.8584	0.57494	1/4	0.61281	0.0078
Sc1	4c	0.26	0.07993	1/4	0.38793	0.0073
Sc2	4c	0.14	0.57494	1/4	0.61281	0.0078
Eu1	4c	0.0024	0.07993	1/4	0.38793	0.0073
Eu2	4c	0.0016	0.57494	1/4	0.61281	0.0078
O1	4c	1	0.07233	1/4	0.07094	0.0146
O2	4c	1	0.2951	1/4	0.31671	0.0185
O3	4c	1	0.37073	1/4	0.00957	0.2533
O4	4c	1	0.47388	1/4	0.80101	0.0692

For Review Only

Table S6. The atomic coordinates, occupancy and isotropic thermal displacement parameters (Å^2) of $SrLu_{1.4}Sc_{0.6}O_4$: $0.004Eu^{2+}$ ceramic.

Atom	Wyck.	S.O.F.	x	y	z	U (Å^2)
Sr1	4c	1	0.24812	1/4	0.6466	0.0024
Lu1	4c	0.6178	0.08076	1/4	0.38781	0.0048
Lu2	4c	0.7782	0.57468	1/4	0.61299	0.0081
Sc1	4c	0.38	0.08076	1/4	0.38781	0.0048
Sc2	4c	0.22	0.57468	1/4	0.61299	0.0081
Eu1	4c	0.0022	0.08076	1/4	0.38781	0.0048
Eu2	4c	0.0018	0.57468	1/4	0.61299	0.0081
O1	4c	1	0.0705	1/4	0.06961	0.0163
O2	4c	1	0.30428	1/4	0.3209	0.0232
O3	4c	1	0.38217	1/4	0.01619	0.1945
O4	4c	1	0.46506	1/4	0.79564	0.0860

For Review Only

Table S7. The atomic coordinates, occupancy and isotropic thermal displacement parameters (Å^2) of $SrLu_{1.2}Sc_{0.8}O_4$: $0.004Eu^{2+}$ ceramic.

Atom	Wyck.	S.O.F.	x	y	z	U (Å^2)
Sr1	4c	1	0.24745	1/4	0.64705	0.0003
Lu1	4c	0.5478	0.08111	1/4	0.38727	0.0083
Lu2	4c	0.6482	0.57554	1/4	0.6132	0.0012
Sc1	4c	0.45	0.08111	1/4	0.38727	0.0083
Sc2	4c	0.35	0.57554	1/4	0.6132	0.0012
Eu1	4c	0.0022	0.08111	1/4	0.38727	0.0083
Eu2	4c	0.0018	0.57554	1/4	0.6132	0.0012
O1	4c	1	0.08002	1/4	0.09167	0.0199
O2	4c	1	0.29741	1/4	0.31779	0.0208
O3	4c	1	0.3643	1/4	0.05289	0.1912
O4	4c	1	0.49509	1/4	0.78294	0.1214

For Review Only

Table S8. The CIE color coordinates and color purity of $Sr(Lu_{1-x}Sc_x)_2O_4$: $0.004Eu^{2+}$ ($0 \leq x \leq 0.4$) PCs.

Red ceramics	Color coordinate	Color purity (%)	Emission peak position (nm)	FWHM (nm)
$SrLu_2O_4$: Eu^{2+}	(0.6256, 0.3738)	79.6	611	73
$SrLu_{1.8}Sc_{0.2}O_4$: Eu^{2+}	(0.6426, 0.3569)	83.3	618	75
$SrLu_{1.6}Sc_{0.4}O_4$: Eu^{2+}	(0.6584, 0.3381)	87.1	625	77
$SrLu_{1.4}Sc_{0.6}O_4$: Eu^{2+}	(0.6722, 0.3224)	90.6	633	79
$SrLu_{1.2}Sc_{0.8}O_4$: Eu^{2+}	(0.6836, 0.3114)	93.5	643	83

For Review Only

Table S9. Thermal conductivity and related parameters of SLS: Eu^{2+} ceramic.

Material	Temperature (℃)	Sizes (mm)	Density (g/cm^3)	Specific heat ($J \cdot g^{-1} \cdot K^{-1}$)	Thermal diffusivity (mm^2/s)	Thermal conductivity ($W \cdot m^{-1} \cdot K^{-1}$)
$SrLu_{1.8}Sc_{0.2}O_4$: Eu^{2+}	22.7	9.9×9.9×2	8.05	0.514	1.973	8.164

For Review Only

Table S10. Color gamut and CIE color coordinates for NTSC 1931 standard, Rec.2020 standard, YAG: Ce^{3+}, and SLS: Eu^{2+}-based laser-driven projection displays.

	CIE color coordinates			Color gamut	
	Red	Green	Blue	NTSC	Rec.2020
NTSC	(0.6810, 0.3086)	(0.2485, 0.7117)	(0.1517, 0.0562)	100%	76.11%
Rec.2020	(0.708, 0.292)	(0.17, 0.797)	(0.131, 0.046)	131.38%	100%
YAG	(0.6521, 0.3474)	(0.3457, 0.6301)	(0.1529, 0.0216)	74.70%	56.85%
SLS	(0.6835,0.3163)	(0.2678, 0.6973)	(0.1529, 0.0216)	100.7%	76.64%

For Review Only

Supplementary Note S1.

Major differences between $Sr(Lu, Sc)_2O_4$: Eu^{2+} and $Sr_3TaO_{5.5}$: Eu^{2+} systems are listed below:

(1) The two hosts possess disparate crystal structures. $Sr_3TaO_{5.5}$ is oxygen-deficient perovskite derivative with non-stoichiometric oxygen content, while $Sr(Lu, Sc)_2O_4$ is stoichiometric layered rare-earth oxide with well-defined cation coordination sites.

(2) Cation substitution mechanism and crystal field modulation rules are unique. We adopt partial substitution of Lu^{3+} by equivalent Sc^{3+} to precisely tailor the unit cell volume, bond lengths, site distortion degree and crystal field splitting. This cation mixing strategy aims to manipulate the nephelauxetic effect and local lattice strain, which was never adopted in the $Sr_3TaO_{5.5}$: Eu^{2+} reported earlier. Establishing a quantitative relationship between Sc doping concentration and luminescence parameters constitutes the core innovation of this work.

(3) Moreover, the tantalate phosphor documented is confined to white-light lighting and lacks suitability for laser-driven display applications [12]. Owing to the engineered local lattice environment, $Sr(Lu, Sc)_2O_4$: Eu^{2+} delivers superior color gamut coverage and color purity by tuning emission wavelength and FWHM, satisfying the rigorous Rec. 2020 criteria for laser-driven projection displays rather than general solid-state lighting.

(4) Previous studies on Eu^{2+}-activated red-emitting ceramics relied on secondary pressing and sintering of pre-synthesized red phosphors, which entailed complicated fabrication procedures [12, 14]. The present work overcomes the preparation bottleneck of conventional red-emitting ceramics. Direct sintering from micron-scale raw materials is realized, yielding ceramics with excellent densification and optoelectronic performance. The proposed strategy offers experimental evidence and instructive references for the development of red luminescent materials, especially red-emitting ceramics targeted for display technologies.

In summary, although both studies focus on Eu^{2+}-doped oxide luminescent materials, the host structure design, lattice modulation strategy, performance characteristics and application orientation are significantly different.

For Review Only

References

1 Zhao J, Sun X, Wang Z. Ce^{3+}/Eu^{2+} doped $SrSc_2O_4$ phosphors: synthesis, luminescence and energy transfer from Ce^{3+} to Eu^{2+}. Chem Phys Lett, 2018, 691: 68-72

2 Richards R, Ciobanu C. Can Hume-Rothery rules predict single-phase high-entropy rocksalt oxide phases? Philos Mag Lett, 2024, 104: 2433726

3 Jin J, Han K, Wang Y, *et al*. Bandgap narrowing in europium(II)-based bromide hybrids toward improved X-ray scintillation and imaging. Chem Mater, 2024, 36: 4813-4820

4 Ali M, Mohamed M, Chen Y, *et al*. Boosting luminescence in oxide phosphors by the vitrifying-devitrifying approach. Nat Commun, 2026, 17: 6176

5 Lin J, Chen S, Ye W, *et al*. Ultra-stable yellow monolithic perovskite quantum dots film for backlit display. Adv Funct Mater, 2024, 34: 2314795

6 Hu T, Gao Y, Molokeev M, *et al*. Eu^{2+} stabilized at octahedrally coordinated Ln^{3+} site enabling red emission in $Sr_3LnAl_2O_{7.5}$ (Ln = Y or Lu) phosphors. Adv Opt Mater, 2021, 9: 2100077

7 Yang Z, Zhao Y, Zhou Y, *et al*. Giant red-shifted emission in $(Sr,Ba)Y_2O_4:Eu^{2+}$ phosphor toward broadband near-infrared luminescence. Adv Funct Mater, 2022, 32: 2103927

8 Li G, Wang Y, Guo H, *et al*. Electronic structure, photoluminescence and phosphorescence properties in $BaSc_2Si_3O_{10}:Eu^{2+}$, RE^{3+} (RE^{3+} = Nd^{3+}, Tm^{3+}, Dy^{3+} and Tb^{3+}) phosphors. J Lumin, 2017, 192: 98-104

9 Zhao M, Zhang Y, Hu Q, *et al*. Eu^{2+} luminescence stabilization at Ln^{3+} sites promoted by interstitial Alkali-Metal defects. Laser Photonics Rev, 2026, 20: e02558

10 Wu L, Sun S, Bai Y, *et al.* Defect-induced self-reduction and anti-thermal quenching in $NaZn(PO_3)_3:Mn^{2+}$ red phosphor. Adv Opt Mater, 2021, 9: 2100870

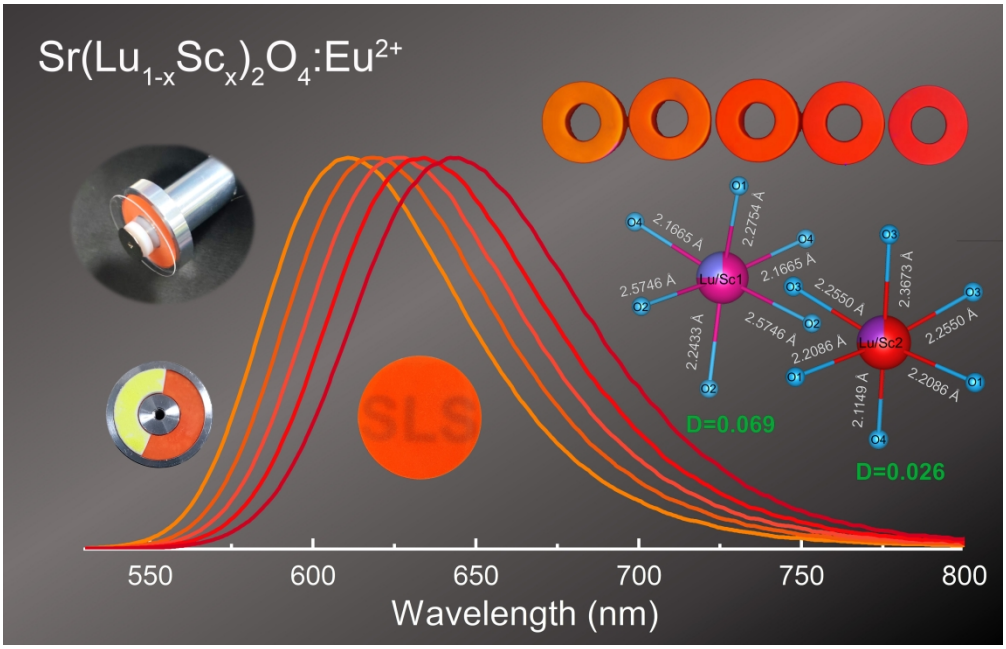
11 Chen W, Wang Y, Liu G, *et al*. Si/Al order and texture orientation optimization of red-emitting $Mg_2Al_4Si_5O_{18}:Eu^{2+}$ ceramics for laser phosphor display. J Materiomics, 2024, 10: 1137-1143

12 Yang Z, de Boer T, Braun P, *et al*. Thermally stable red-emitting oxide ceramics for laser lighting. Adv Mater, 2023, 35: 2301837

13 Chen W, Wang Y, Xu J, *et al*. Red-emitting cordierite ceramic enabling general healthy warm white laser lighting. Laser Photonics Rev, 2024, 18: 2300963

14 Tian R, Wang Q, Li S, *et al*. Efficient $Sr_{0.5}Ca_{0.5}AlSiN_3:Eu^{2+}$ red-emitting ceramics for high-power solid-state lighting. J Mater Sci Technol, 2025, 210: 179-187

For Review Only



1666x1066mm (72 x 72 DPI)

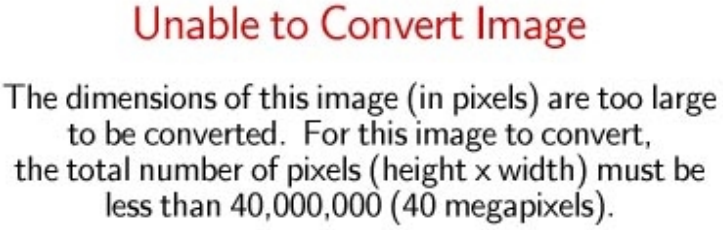

Unable to Convert Image
The dimensions of this image (in pixels) are too large to be converted. For this image to convert, the total number of pixels (height x width) must be less than 40,000,000 (40 megapixels).

Figure 1

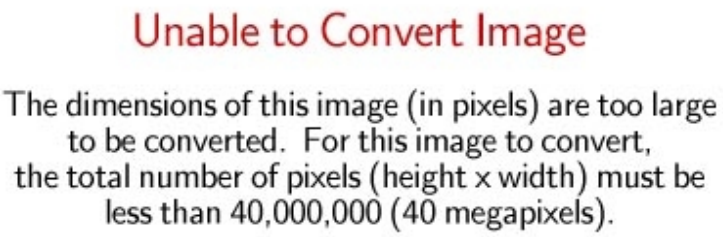

Unable to Convert Image
The dimensions of this image (in pixels) are too large to be converted. For this image to convert, the total number of pixels (height x width) must be less than 40,000,000 (40 megapixels).

Figure 2

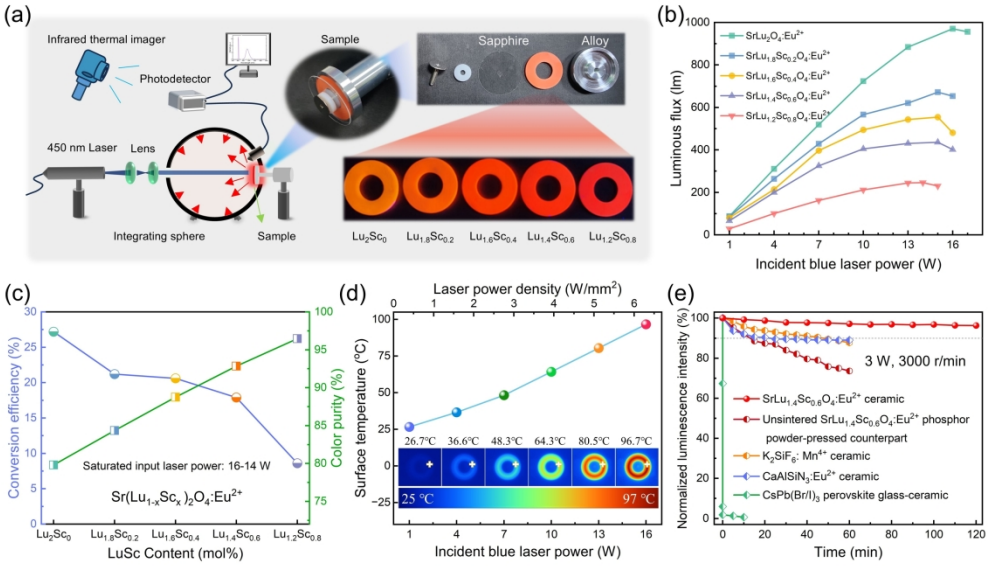


Figure 3

249x143mm (300 x 300 DPI)

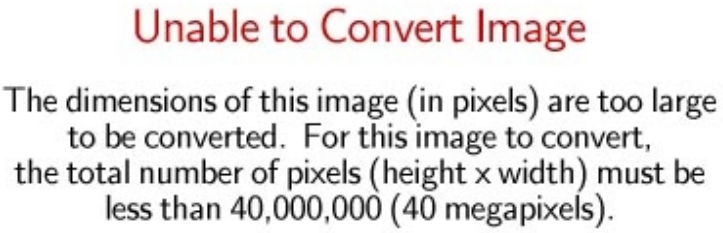

Unable to Convert Image
The dimensions of this image (in pixels) are too large to be converted. For this image to convert, the total number of pixels (height x width) must be less than 40,000,000 (40 megapixels).

Figure 4